Physics of Fluids

Statistical properties of three-dimensional Hall magnetohydrodynamics turbulence

Cite as: Phys. Fluids **34**, 095135 (2022); https://doi.org/10.1063/5.0107434
Submitted: 05 July 2022 • Accepted: 28 August 2022 • Accepted Manuscript Online: 01 September 2022 • Published Online: 27 September 2022

Sharad K. Yadav, Hideaki Miura and Rahul Pandit

Physics of Fluids ARTICLE scitation.org/journal/phf

Statistical properties of three-dimensional Hall magnetohydrodynamics turbulence

Cite as: Phys. Fluids **34**, 095135 (2022); doi: 10.1063/5.0107434
Submitted: 5 July 2022 · Accepted: 28 August 2022 ·
Published Online: 27 September 2022

Sharad K. Yadav,[1,a)] Hideaki Miura,[2,b)] and Rahul Pandit[3,c)]

AFFILIATIONS

[1]Department of Physics, Sardar Vallabhbhai National Institute of Technology (SVNIT), Surat 395007, Gujarat, India
[2]National Institute for Fusion Science (NIFS), Toki, Gifu 509-5292, Japan
[3]Centre for Condensed Matter Theory, Department of Physics, Indian Institute of Science (IISc), Bangalore 560012, India

[a)]**Author to whom correspondence should be addressed:** sharadyadav@phy.svnit.ac.in and sharadky@gmail.com
[b)]**Electronic mail:** miura.hideaki@nifs.ac.jp
[c)]**Electronic mail:** rahul@iisc.ac.in

ABSTRACT

The three-dimensional (3D) Hall magnetohydrodynamics (HMHD) equations are often used to study turbulence in the solar wind. Some earlier studies have investigated the statistical properties of 3D HMHD turbulence by using simple shell models or pseudospectral direct numerical simulations (DNSs) of the 3D HMHD equations; these DNSs have been restricted to modest spatial resolutions and have covered a limited parameter range. To explore the dependence of 3D HMHD turbulence on the Reynolds number Re and the ion-inertial scale d_i, we have carried out detailed pseudospectral DNSs of the 3D HMHD equations and their counterparts for 3D MHD ($d_i = 0$). We present several statistical properties of 3D HMHD turbulence, which we compare with 3D MHD turbulence by calculating (a) the temporal evolution of the energy-dissipation rates and the energy; (b) the wave-number dependence of fluid and magnetic spectra; (c) the probability distribution functions of the cosines of the angles between various pairs of vectors, such as the velocity and the magnetic field; and (d) various measures of the intermittency in 3D HMHD and 3D MHD turbulence.

I. INTRODUCTION

Electrically conducting fluids can exhibit turbulence that is characterized not only by fluctuations in the fluid velocity and the vorticity but also in the magnetic field and the current. At the simplest level, such fluids can be modeled by using the equations of magnetohydrodynamics (MHD).[1–9] Examples of such conducting-fluid flows can be found in liquid metals, in the interiors of planets or in laboratories,[10–13] solar or stellar settings,[1–4] the solar wind,[14–19] and the interstellar medium.[1–4,20] The MHD description of a plasma is based on a single-fluid approximation. However, in plasmas like the solar wind, this single-fluid assumption is not valid, especially at small scales comparable to or smaller than the ion-inertial length scale $d_i = c/\omega_{pi}$, with c the velocity of light and the ion plasma frequency $\omega_{pi} \equiv \sqrt{4\pi n_i Z^2 e^2/m_i}$, where Z is the charge state, n_i is the ion density, and m_i is the mass of the ion. Hall magnetohydrodynamics (HMHD) is a simplified fluid description of a plasma that accounts for two-fluid effects, to some extent; HMHD includes the Hall term in the Ohm's law;[21–46] and it reduces to MHD if $d_i = 0$. Shell models have also been developed to study the statistical properties of HMHD turbulence.[38,47] The HMHD partial differential equations (PDEs) pose several challenges for mathematicians, who study the regularity properties of solutions of these PDEs,[48,49] for fluid dynamicists and statistical mechanicians, who seek to characterize the statistical properties of HMHD turbulence, and for astrophysicists, who use these PDEs to model turbulence in astrophysical systems such as the solar wind. The solar wind[2,14–17,50–58] has been described as a turbulence laboratory,[52] for it is in a highly turbulent state: the magnetic Reynolds number Re_M lies in the range $10^5 \lesssim \mathrm{Re}_M \lesssim 10^9$ and the magnetic Prandtl number $\mathrm{Pr}_M \simeq 1$; the kinetic- and magnetic-energy spectra, $E_u(k)$ and $E_b(k)$, respectively, extend over many decades of the wave number k; for time-domain measurements, k is replaced by the frequency f. Satellite observations of solar-wind-plasma turbulence[15,54–61] have shown that, in the inertial range, $E_u(f) \sim f^{-\alpha}$, with $\alpha \simeq 5/3$, the scaling exponent that follows from the Kolmogorov hypotheses[62] of 1941 (henceforth K41). In contrast, the magnetic-energy spectrum has two different scaling or inertial ranges (henceforth, we refer to them as the *inertial* and *second-inertial* ranges): (i) for $f_I \ll f \ll f_{ci}$, $E_b(f) \sim f^{-\alpha}$, where

the frequency f_I is related inversely to the integral length scale of the turbulence, f_{ci}, the ion-cyclotron frequency is related inversely to d_i and $\alpha \simeq 5/3$ is consistent with the K41 value; (ii) for $f_{ci} \ll f \ll f_d$, where the frequency f_d is related inversely to the dissipation length scale at which viscous losses become significant, $E_b(f) \sim f^{-\alpha_1}$, with α_1 in the range $1 \lesssim \alpha_1 \lesssim 4$. The solar wind is unlike a well-controlled experiment in a laboratory, so it is not surprising that spectral exponents show a range of values (see, e.g., Ref. 63, Figs. 5 in Ref. 64, and 3 of Ref. 58); this variability of exponents has been attributed to transients, unsteady conditions, anisotropies, and effects that lie beyond an incompressible-MHD description.[64–66] Solar-wind-turbulence data have also been analyzed to uncover (a) intermittency and multiscaling of velocity and magnetic-field structure functions[54,67] and (b) the alignment of velocity and magnetic-field fluctuations.[16] In particular, the study of Ref. 54 has found structure–function multiscaling (simple scaling), in the first (second) frequency range mentioned above. The magnetosheath is another near-Earth space plasma; for a comparison of plasma turbulence in the solar wind and in the magnetosheath, we refer the reader to Refs. 58 and 61.

There has been a steady stream of theoretical studies and direct numerical simulations (DNSs) of HMHD;[21–44,68] most of these concentrate on three-dimensional (3D) HMHD or related shell-model or large-eddy-simulation investigations. These studies yield a spectral exponent $\alpha \simeq 5/3$, which is consistent with K41; however, the values of the spectral exponent α_1, suggested in different theoretical and DNS studies, lie in a large range: $1 \lesssim \alpha_1 \lesssim 5.5$; clearly, it is more challenging to develop an understanding of 3D HMHD turbulence than of its MHD and fluid counterparts. Some of these works (see, e.g., Refs. 33, 37, 39, and 43) have provided phenomenological arguments for the values of α_1 that have been obtained in different DNSs. It has been suggested that, in addition to d_i and the Reynolds and Prandtl numbers, the statistical properties of 3D HMHD might well depend on other parameters like the Alfvén number, which is the ratio of kinetic and magnetic energies. Furthermore, DNSs have explored (a) the intermittency and multiscaling of velocity and magnetic-field structure functions[30,38,56,67,69] and (b) the alignment of velocity and magnetic-field fluctuations.[16]

Given the uncertainties in spectral exponents and the statistical properties of 3D HMHD turbulence, it behooves us to initiate systematic investigations of these properties of the type that have been carried out for 3D MHD turbulence.[8,70] We present such a study. In particular, we use extensive pseudospectral DNSs, with two different types of initial conditions [henceforth, the initial conditions A and B (see below)], to obtain the statistical properties of turbulence in the unforced 3D HMHD equations; a comparison of such properties provides valuable insights into the initial-condition dependence of the exponent α_1 and multiscaling exponents. Before we present the details of our work, we provide a qualitative overview of the principal results from our DNSs:

- Spectra: In our 3D MHD and 3D HMHD DNSs, in the inertial range mentioned above, both

$$E_u(k) \sim k^{-\alpha}; \quad E_b(k) \sim k^{-\alpha}; \tag{1}$$

the value of the spectral exponent α is consistent with the K41 result 5/3. In the second-inertial range, with lengths l in the range $d_i \ll l \ll \eta_d^b$, where η_d^b is the magnetic-dissipation length scale,

$$E_b(k) \sim k^{-\alpha_1}, \tag{2}$$

with the value of α_1 consistent with (A) 11/3, for the initial condition A, and (B) 7/3, for the initial condition B (see Sec. II for precise definitions of these spectra and the initial conditions). We also explore the k-dependence of other spectra and of the wavenumber-dependent Alfvén number $E_b(k)/E_u(k)$ for these two initial conditions.

- Probability distribution functions (PDFs):
- We compute the PDFs of the cosines of the angles between various fields, such as the velocity $\mathbf{u}$, vorticity $\boldsymbol{\omega} = \nabla \times \mathbf{u}$, magnetic field $\mathbf{b}$, and current density $\mathbf{j} = \nabla \times \mathbf{b}$, to highlight the importance of the Hall term in suppressing the tendency of alignment (or antialignment) of these fields for both the initial conditions (A) and (B).
- We also explore intermittency in 3D HMHD turbulence (and compare it with its 3D MHD counterpart) by calculating the PDFs of the velocity and magnetic-field increments as a function of the separation length scale l. We find evidence of small-scale intermittency in our 3D HMHD plasma turbulence DNSs (as in 3D MHD plasma turbulence DNSs); our DNSs, especially those for the initial condition (A), show clearly that intermittency is suppressed significantly in the second scaling range of 3D HMHD plasma turbulence, in agreement with the results of solar-wind measurements.[54]
- Structure functions: We compute the l-dependence of velocity and magnetic-field structure functions and, therefrom, their order-p multiscaling exponents ζ_p^u and ζ_p^b, respectively. In the inertial range, ζ_p^u and ζ_p^b are nonlinear, monotone increasing functions of p; this is a clear signature of multiscaling. By contrast, in the second-inertial range, ζ_p^u and ζ_p^b increase linearly with p, a hallmark of simple scaling; this linear dependence is in consonance with solar-wind results.[54]

The remainder of this paper is organized as follows. In Sec. II, we present the 3D HMHD PDEs (Subsection II A), the pseudospectral DNSs we employ to solve these PDEs, and the definitions of various statistical measures (Subsection II B) that we use to characterize 3D HMHD turbulence. In Sec. III, we provide results from our DNSs in three subsections: in Subsection III A, we discuss the temporal evolution of the energy-dissipation rates and the energy and the wavenumber dependence of spectra, such as $E_u(k)$ and $E_b(k)$. In Subsection III B, we compute PDFs of the cosines of the angles between the following pairs of vectors: $\{\mathbf{u}, \mathbf{b}\}$, $\{\mathbf{u}, \mathbf{j}\}$, $\{\mathbf{u}, \boldsymbol{\omega}\}$, $\{\mathbf{b}, \mathbf{j}\}$, $\{\mathbf{b}, \boldsymbol{\omega}\}$, and $\{\boldsymbol{\omega}, \mathbf{j}\}$; by using these PDFs, we quantify the degree of alignment between these pairs of vectors. In Subsection III C, we present some joint PDFs. In Subsection III D, we characterize intermittency in 3D HMHD turbulence by examining the l dependence PDFs of velocity- and magnetic-field increments and the order-p structure functions of these increments. Finally, we discuss the implications of our study in Sec. IV.

II. MODEL AND METHODS

We begin with the 3D HMHD PDEs (Subsection II A); then, we present an outline of our pseudospectral DNS method and the definitions of statistical measures (Subsection II B) for 3D HMHD turbulence.

A. Basic equations

Three-dimensional (3D) HMHD is described by the following set of coupled PDEs for $\mathbf{u}$ and $\mathbf{b}$:

$$\frac{\partial \mathbf{u}}{\partial t} + (\mathbf{u}\cdot\nabla)\mathbf{u} = -\nabla\bar{p} + (\mathbf{b}\cdot\nabla)\mathbf{b} + \nu\nabla^2\mathbf{u} + \mathbf{f_u}; \tag{3}$$

$$\frac{\partial \mathbf{b}}{\partial t} = \nabla\times(\mathbf{u}\times\mathbf{b} - d_i\mathbf{j}\times\mathbf{b}) + \eta\nabla^2\mathbf{b} + \mathbf{f_b}; \tag{4}$$

$$\nabla\cdot\mathbf{u} = 0; \quad \nabla\cdot\mathbf{b} = 0. \tag{5}$$

Equation (3) is the momentum equation; this includes a contribution from the Lorentz force $\mathbf{j}\times\mathbf{b}$, with the current density $\mathbf{j} = \nabla\times\mathbf{b}$, which can be separated into the magnetic-tension term $(\mathbf{b}\cdot\nabla)\mathbf{b}$ and the magnetic pressure, which we combine with the pressure p to obtain the total pressure $\bar{p} \equiv p + |\mathbf{b}|^2/4\pi$. The induction equation (4) uses the generalized form of Ohm's law, which includes the Hall term $\sim\mathbf{j}\times\mathbf{b}$, whose coefficient d_i is the ion-inertial length; η and ν are, respectively, the kinematic viscosity and the magnetic resistivity (or diffusivity); $\mathbf{f_u}$ and $\mathbf{f_b}$ are the forcing terms. The Poisson equation for $\bar{p}$ follows from the divergence of Eq. (3) and the incompressibility condition $\nabla\cdot\mathbf{u} = 0$:

$$\nabla^2\bar{p} = \nabla\cdot[(\mathbf{b}\cdot\nabla)\mathbf{b} - (\mathbf{u}\cdot\nabla)\mathbf{u}] + \nabla\cdot\mathbf{f_u}. \tag{6}$$

We study decaying HMHD turbulence, so we set $\mathbf{f_u} = 0$ and $\mathbf{f_b} = 0$. Thus, the final form for the pressure-Poisson equation is

$$\nabla^2\bar{p} = \nabla\cdot\big[(\mathbf{b}\cdot\nabla)\mathbf{b} - (\mathbf{u}\cdot\nabla)\mathbf{u}\big]. \tag{7}$$

B. Direct numerical simulations and statistical measures

We solve Eqs. (3) and (4) by using the pseudospectral method in a cubical domain of side $L = 2\pi$, with periodic boundary conditions (see, e.g., Ref. 8 for 3D MHD). We remove the aliasing error, because of the nonlinear terms, by using the 2/3 dealiasing method. For time integration, we employ the second-order slaved, Adams–Bashforth scheme.

We perform four sets of simulations, Run1, Run2, Run3, and Run4, in which the initial energy spectra (initial condition A) for the velocity and magnetic fields are as follows:

$$E_u^0(k) = E_b^0(k) = E^0 k^4 \exp(-2k^2), \tag{8}$$

where $E^0 \simeq 10$ is the initial amplitude in our DNSs. For the DNSs Run5a, Run5b, and Run5c, these initial spectra (initial condition B) are

$$E_u^0(k) = E_b^0(k) = E^0 k^2 \exp(-2k^2). \tag{9}$$

The phases of the Fourier modes of the velocity and magnetic fields in Eqs. (8) and (9) are distributed randomly and uniformly on the interval $[0, 2\pi)$. Some data from the DNSs Run5a, Run5b, and Run5c have been published[34] in a different context.

Given the uncertainties in spectral exponents and the statistical properties of 3D HMHD turbulence, it is important to investigate systematically if these properties depend on initial conditions. Therefore, we used two types of initial conditions (A and B) that are often used in studies of decaying MHD turbulence.[8] We carry out a detailed comparison of results from Run1–Run4 and Run5a–Run5c. The values of various parameters from our DNSs are listed in Table I.

To characterize the statistical properties of 3D MHD and 3D HMHD turbulence, we compute the following (cf. Ref. 8 for 3D MHD turbulence):

- At time t, we obtain the kinetic energy, magnetic energy, kinetic-energy-dissipation rate, magnetic-energy-dissipation rate, and pressure spectra, which are, respectively,

$$\begin{aligned} E_u(k,t) &\equiv \sum_{k-\frac{1}{2}\le k'\le k+\frac{1}{2}} |\tilde{\mathbf{u}}(\mathbf{k}',t)|^2; \\ E_b(k,t) &\equiv \sum_{k-\frac{1}{2}\le k'\le k+\frac{1}{2}} |\tilde{\mathbf{b}}(\mathbf{k}',t)|^2; \\ \epsilon_u(k,t) &= \nu k^2 E_u(k,t); \\ \epsilon_b(k,t) &= \eta k^2 E_b(k,t); \\ P(k,t) &\equiv \sum_{k-\frac{1}{2}\le k'\le k+\frac{1}{2}} |\tilde{\bar{p}}(\mathbf{k}',t)|^2; \end{aligned} \tag{10}$$

here, tildes denote spatial Fourier transforms, and $k' \equiv |\mathbf{k}'|$; we compute the time evolution of different energies and dissipation rates by summing the corresponding spectrum over the wave number k; e.g., $E_u(t) = \sum_k E_u(k,t)$. In the inertial and second-inertial

TABLE I. Parameters in our DNSs Run1, Run2, Run3, Run4, Run5a, Run5b, and Run5c: N^3 is the number of collocation points; ν is the kinematic viscosity; Pr_M is the magnetic Prandtl number; d_i is the ion-inertial length (it is 0 for the MHD runs); δt is the time step; u_{rms}, l_I, λ, and Re_λ are the root-mean-square velocity, the integral scale, the Taylor microscale, and the Taylor-microscale Reynolds number, respectively. Most of these quantities are obtained at the cascade-completion time t_c (see the text); η_d^u and η_d^b are, respectively, the Kolmogorov dissipation length scales for the velocity and magnetic fields. k_{max} is the magnitude of the largest wave numbers in our DNSs ($k_{max} \simeq 85.33$, 170.67, and 343.33 for N = 256, 512, and 1024, respectively).

Run	N	ν	Pr_M	d_i	δt	u_{rms}	l_I	λ	Re_λ	t_c	$k_{max}\eta_d^u$	$k_{max}\eta_d^b$
Run1	256	10^{-3}	1	0.0	5.0×10^{-4}	0.29	1.193	0.13	39	6.76	2.09	1.89
Run2	256	10^{-3}	1	0.05	5.0×10^{-4}	0.13	0.12	0.128	17	7.4	2.1	1.8
Run3	512	5.0×10^{-4}	1	0.0	10^{-4}	0.28	0.29	0.25	142	9.13	1.82	1.65
Run4	512	5.0×10^{-4}	1	0.05	10^{-4}	0.29	0.32	0.28	165	9.65	1.8	1.6
Run5	1024	5.0×10^{-4}	1	0.0	10^{-4}	1.0	0.35	0.07	143	0.5	1.53	1.37
Run5b	1024	5.0×10^{-4}	1	0.025	10^{-4}	1.0	0.37	0.08	153	0.5	1.60	1.30
Run5c	1024	5.0×10^{-4}	1	0.05	10^{-4}	1.0	0.36	0.09	176	0.5	1.71	1.25

ranges mentioned above, these spectra show power-law dependences on k, which we elucidate below.

- We compute PDFs of the cosine of the angles between the following pairs of vectors, to characterize the degree of alignment between them: $\{\mathbf{u},\mathbf{b}\}$, $\{\mathbf{u},\mathbf{j}\}$, $\{\mathbf{u},\boldsymbol{\omega}\}$, $\{\mathbf{b},\mathbf{j}\}$, $\{\mathbf{b},\boldsymbol{\omega}\}$, and $\{\boldsymbol{\omega},\mathbf{j}\}$.
- To characterize multifractality and the intermittency, we calculate the order–p, equal-time longitudinal structure functions at time t:

$$S_p^a(l) = \langle |\delta a_{||}(\mathbf{x},l)|^p \rangle; \quad \delta a_{||}(\mathbf{a},l) = \left[\mathbf{a}(\mathbf{x}+\mathbf{l},\mathbf{t}) - \mathbf{a}(\mathbf{x},\mathbf{t})\cdot\frac{\mathbf{l}}{l}\right]; \tag{11}$$

here, $\mathbf{a}_{||}$ is the longitudinal component of $\mathbf{a}$, which is $\mathbf{u}$ or $\mathbf{b}$ for velocity and magnetic-field structure functions, and $\delta a_{||}(\mathbf{a},l)$ is the longitudinal component of its increment; we suppress t in the arguments of structure functions for notational convenience. In the inertial range,

$$S_p^u(l) \sim l^{\zeta_p^u}; \quad S_p^b(l) \sim l^{\zeta_p^b}; \tag{12}$$

ζ_p^u and ζ_p^b are the velocity and magnetic-field multiscaling exponents of order p. As we show below, in 3D HMHD turbulence, the magnetic-field spectra and structure functions exhibit two different scaling regions called *inertial* and *second-inertial* regions; e.g.,

$$d_i \ll l \ll L; \quad S_p^b(l) \sim l^{\zeta_p^{b,1}}; \quad \eta_d^b \ll l \ll d_i; \quad S_p^b(l) \sim l^{\zeta_p^{b,2}}; \tag{13}$$

here, $\zeta_p^{b,1}$ and $\zeta_p^{b,2}$ are the multiscaling exponents in these two scaling regions. To study intermittency, we also compute PDFs of velocity and magnetic field increments and the hyperflatnesses

$$F_6^a(l) = S_6^a(l)/\left[S_2^a(l)\right]^3. \tag{14}$$

III. RESULTS

We present the results of our DNSs in four subsections: In Subsection III A, we discuss the temporal evolution of the energy-dissipation rates and the energy; we then present the spectra that we have defined above. In Subsection III B, we compute probability distribution functions (PDFs) of the cosine of the angles between the following pairs of vectors: $\{\mathbf{u},\mathbf{b}\}$, $\{\mathbf{u},\mathbf{j}\}$, $\{\mathbf{u},\boldsymbol{\omega}\}$, $\{\mathbf{b},\mathbf{j}\}$, $\{\mathbf{b},\boldsymbol{\omega}\}$, and $\{\boldsymbol{\omega},\mathbf{j}\}$; these PDFs help us quantify the degree of alignment between these pairs. In Subsection III C, we present the joint PDFs of the invariants of the velocity-gradient tensor and the moduli of the vorticity and the current. In Subsection III D, we characterize intermittency in 3D HMHD turbulence by examining PDFs of velocity and magnetic-field increments and the l dependences of order-p structure functions of these increments.

A. Temporal evolution and spectra

In Fig. 1(a), we display the time evolution of the kinetic-energy dissipation rate (blue curves), the magnetic-energy dissipation rate (red curves), and total-energy dissipation rate (black curves) from Run1 (dashed lines) and Run2 (solid lines) for 3D MHD and 3D HMHD turbulence, respectively. We remark that these dissipation rates increase sharply, up until a cascade-completion time τ_c, and then they decay slowly. The peak positions are nearly the same for all these curves; the peaks for Run1 occur marginally earlier than they do in Run2. In Fig. 1(b), we present the time dependence of the fluid, magnetic, and total energies in simulations Run1 and Run2. Figures 1(c) and 1(d) are the counterparts of 1(a) and 1(b) for Run3 and Run4. Figures 1(e) and 1(f) display the spectra of the kinetic-energy-dissipation rate and the magnetic-energy-dissipation rate, respectively, at τ_c for Run1, Run2, Run3, Run4, Run5a, Run5b, and Run5c; the well-developed peaks in these spectra show that our DNSs are well resolved; we also summarize this in Table I, which shows that $k_{max}\eta_d^u > 1$ and $k_{max}\eta_d^b > 1$ for all these runs.

In Fig. 2, we show the compensated spectra of the kinetic energy and the magnetic energy $E_u(k)$ (open circles) $E_b(k)$ (asterisks), respectively, which we have obtained from our DNSs at the cascade-completion time τ_c. Specifically, we present log–log (base 10) plots vs the wave number k of the following: (a) $k^{5/3}E_u(k)$ (lower two curves) and $k^{11/3}E_b(k)$ (upper two curves) from *Run*3 (red curves) and *Run*4 (blue curves), with solid black lines indicating different power-law regions [Fig. 2(a)]; (b) $k^{5/3}E_u(k)$ (lower three curves) and the compensated magnetic energy spectra $k^{11/3}E_b(k)$ (upper three curves) from Run5a (blue curves), Run5b (red curves), and Run5c (black curves); (c) the wave-number-dependent Alfvén ratios $E_b(k)/E_u(k)$ for Run3, Run4, Run5a, Run5b, and Run5c [Fig. 2(c)]; the wavenumber $k_i \propto 1/d_i$. From these plots, we conclude that the spectral exponents [Eqs. (1) and (2)] are consistent with

$$\begin{aligned} \alpha &\simeq 5/3, \quad \text{the K41 value;} \\ \alpha_1 &\simeq 11/3 \quad \text{for initial condition A;} \\ \alpha_1 &\simeq 7/3 \quad \text{for initial condition B.} \end{aligned} \tag{15}$$

The values of α_1 are clearly different for initial condition A [Eq. (8) and Run2 and Run4] and initial condition B [Eq. (9) and Run5b–Run5c]. These differences stem, in part, from the disparities in the wave-number-dependent Alfvén ratios $E_b(k)/E_u(k)$ [Fig. 2(c)] and, as we show in Subsection III B, in the alignment PDFs of various vector fields. In all our runs, the ratio $E_b(k)/E_u(k)$ lies in the range 1–2 at small values of $k \lesssim k_i \propto d_i$; for $k_i < k < k_{max}$, this ratio is different for different runs. For example, for Run5c, $E_b(k)/E_u(k)$ remains nearly constant up until $k \sim 60$, i.e., up until $\simeq 3k_i$ *beyond* k_i; by contrast, for Run4, this ratio rises rapidly, with increasing k, at large k. For Run5c, this near constancy, with $E_b(k)/E_u(k)$ in the range of 1–2, indicates approximate equipartition of the energies in the velocity and magnetic fields. It has been recognized[39] that such equipartition suggests $\alpha_1 = 7/3$. In contrast, $\alpha_1 = 11/3$ can be obtained by equating τ_{nl} and τ_h and by using $E_b/E_u = d_i^2k^2$, where τ_{nl} is the energy-transfer because of the nonlinear term in the momentum equation and τ_h is the energy-transfer time because of the Hall term in the induction equation.[39]

Furthermore, to understand these two different scaling behaviors in our HMHD DNSs, we have computed the magnetic polarization[41]

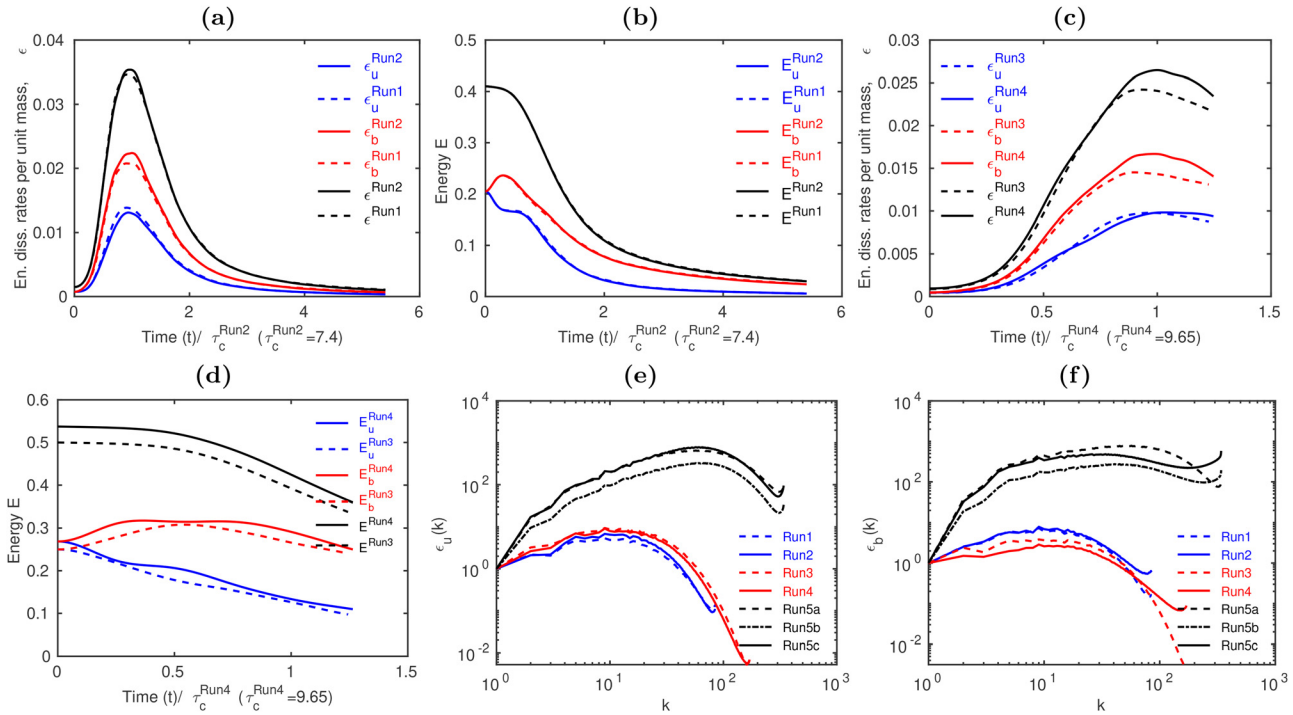

FIG. 1. Plots vs the scaled time t of (a) the kinetic-energy dissipation rate ϵ_u (blue curves), magnetic-energy dissipation rate ϵ_b (red curves), and the total-energy dissipation rate ϵ (black curves) for Run1 (dashed lines) and Run2 (solid lines) and (b) the kinetic energy E_u (blue curve), magnetic energy E_b (red curve), and the total energy E (black curve) for Run1 (dashed lines) and Run2 (solid lines). (c) and (d) are, respectively, the counterparts of (a) and (b) for Run3 and Run4. Log–log (base 10) plots vs the wave number k of (e) the kinetic-energy-dissipation-rate spectra $\epsilon_u(k)$ and (f) the magnetic-energy-dissipation-rate spectra $\epsilon_b(k)$ from Run1 (blue-dashed curve), Run2 (blue-solid curve), Run3 (red-dashed curve), Run4 (red-solid curve), Run5a (black-dashed curve), Run5b (black-dashed-dotted curve), and Run5c (black-solid curve).

$$P_m(k) = \sigma_m(k)\sigma_c(k),$$
$$\sigma_m(k) = \frac{\tilde{\mathbf{A}}\cdot\tilde{\mathbf{b}}^* + \tilde{\mathbf{A}}^*\cdot\tilde{\mathbf{b}}}{2|\tilde{\mathbf{A}}||\tilde{\mathbf{b}}|}, \qquad (16)$$
$$\sigma_c(k) = \frac{\tilde{\mathbf{u}}\cdot\tilde{\mathbf{b}}^* + \tilde{\mathbf{u}}^*\cdot\tilde{\mathbf{b}}}{2|\tilde{\mathbf{u}}||\tilde{\mathbf{b}}|},$$

where $\mathbf{A}$ is the magnetic vector potential, $\tilde{\cdot}$ denotes the spatial Fourier transform, and * is the complex conjugation. $\sigma_m(k)$ and $\sigma_c(k)$ are averaged over shells of radius k in Fourier space [like the spectra in Eq. (10)]. Hall MHD supports both right R and left L circularly polarized waves, for which $P_m = +1$ and $P_m = -1$, respectively. We follow Ref. 41, designate by R and L fluctuations for which $P_m > 0$ and

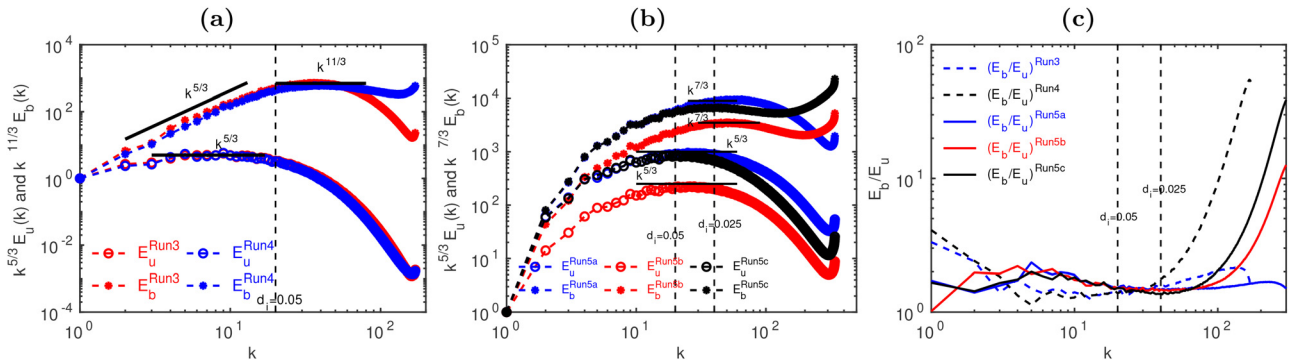

FIG. 2. Log–log (base 10) plots vs the wave number k of (a) the compensated kinetic energy spectra $k^{5/3}E_u(k)$ (lower two curves) and the compensated magnetic energy spectra $k^{11/3}E_b(k)$ (upper two curves) from Run3 (red curves) and Run4 (blue curves); solid black lines indicate different power-law regions; (b) the compensated kinetic energy spectra $k^{5/3}E_u(k)$ (lower three curves) and the compensated magnetic energy spectra $k^{7/3}E_b(k)$ (upper three curves) from Run5a (blue curves), Run5b (red curves), and Run5c (black curves); solid black lines indicate different power-law regions; (c) the wave-number-dependent Alfvén ratios $(E_b(k)/E_u(k))$ for Run3, Run4, Run5a, Run5b, and Run5c. We compute these spectra at the cascade-completion time τ_c and the wavenumber $k_i \propto 1/d_i$.

$P_m < 0$, respectively, and define the following energy spectra for these fluctuations and their sum:

$$E_{R,L}(k,t) \equiv [E_u(k,t) + E_b(k,t)]_{R,L};$$
$$E_T(k,t) \equiv [E_R(k,t) + E_L(k,t)]. \quad (17)$$

In Fig. 3(a), we plot vs k, for Run5c, the fractions $E_L(k)/E_T$ and E_R/E_T of the energy stored in $L-$ and $R-$ polarized waves, respectively; this plot clearly shows the spontaneous chiral symmetry breaking of HMHD turbulence that is discussed in Ref. 41. In Fig. 3(b), we depict compensated magnetic-energy spectra, for Run5c, for the fluctuations with (i) $P_m > 0$ (L), (ii) $P_m \geq 0.5$ (L), and (iii) $P_m < 0$ (R); the first two of these spectra are compensated with $k^{11/3}$, whereas the third is compensated with $k^{7/3}$. These compensated spectra indicate $k^{-7/3}$ and $k^{-11/3}$ scaling forms in the second-inertial region of HMHD plasma turbulence for R and L fluctuations, respectively. In Figs. 3(c) and 3(d), we give the Run4 counterparts of 3(a) and 3(b); here too, we obtain $k^{-7/3}$ and $k^{-11/3}$ scaling forms in the second-inertial region of HMHD plasma turbulence for R and L fluctuations, respectively. We expect the $k^{-11/3}$ region to be more prominent than it is here in very-high-resolution DNSs.

The initial energy spectra in Eqs. (8) and (9) do not specify the initial condition completely: the initial phases of $\tilde{\mathbf{u}}(\mathbf{k})$ and $\tilde{\mathbf{b}}(\mathbf{k})$ must also be given. We now explore the sensitivity of our results to this choice of phases, for the illustrative case of Run2, by taking four different choices of random phases for these Fourier modes of the velocity and magnetic fields; we label these four runs Run2a, Run2b, Run2c, and Run2d. We display illustrative results from these simulations in Figs. 4 and 5. In Fig. 4, we present plots vs time of various energy dissipation rates and energies; although the qualitative t-dependences of these plots are the same for Run2a–Run2d, there are distinct quantitative differences between them. By contrast, the scaling behaviors of the kinetic- and magnetic-energy spectra are not affected significantly by the choice of the initial phases as we can see by comparing the plots in Fig. 5.

B. Probability distribution functions

In Fig. 6, we display, at the cascade-completion time τ_c, the PDFs of the cosines of the angles between the following pairs of vectors: $\{\mathbf{u}, \mathbf{b}\}$, $\{\mathbf{u}, \mathbf{j}\}$, $\{\mathbf{u}, \boldsymbol{\omega}\}$, $\{\mathbf{b}, \mathbf{j}\}$, $\{\mathbf{b}, \boldsymbol{\omega}\}$, and $\{\boldsymbol{\omega}, \mathbf{j}\}$, for Run3 (blue curve) and Run4 (red curve). We present their counterparts for Run5a (blue curve), Run5b (red curve), and Run5c (black curve) in Fig. 7. In Figs. 6 and 7, the blue curves are from the MHD runs Run3 and Run5a (see Table I).

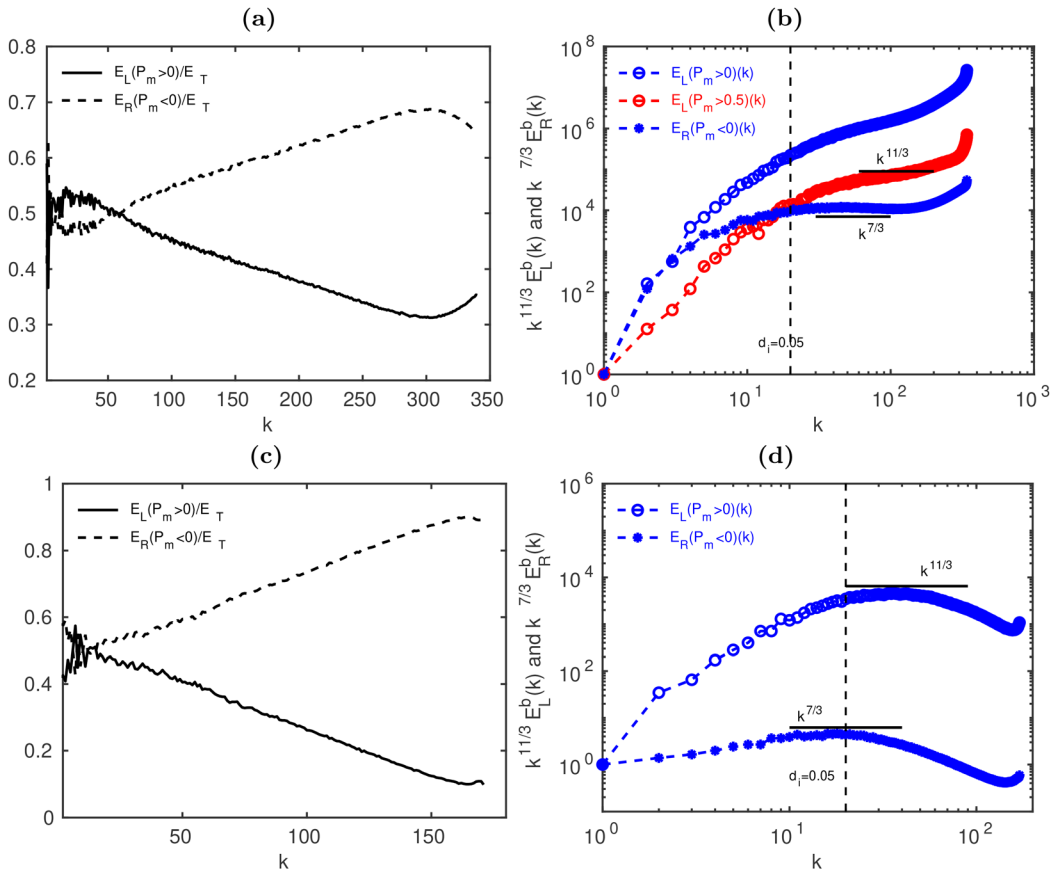

FIG. 3. Run5c: Plots of the energy ratios (see the text for its definition) (a) E_L/E_T (solid curve) and E_R/E_T (dashed curve) and (b) compensated magnetic energy spectra for fluctuations with (see the text) $P_m > 0$ (blue curve), $P_m \geq 0.5$ (red curve), and $P_m < 0$ (blue curve). In (c) and (d), we present the counterparts of (a) and (b), respectively, for Run4.

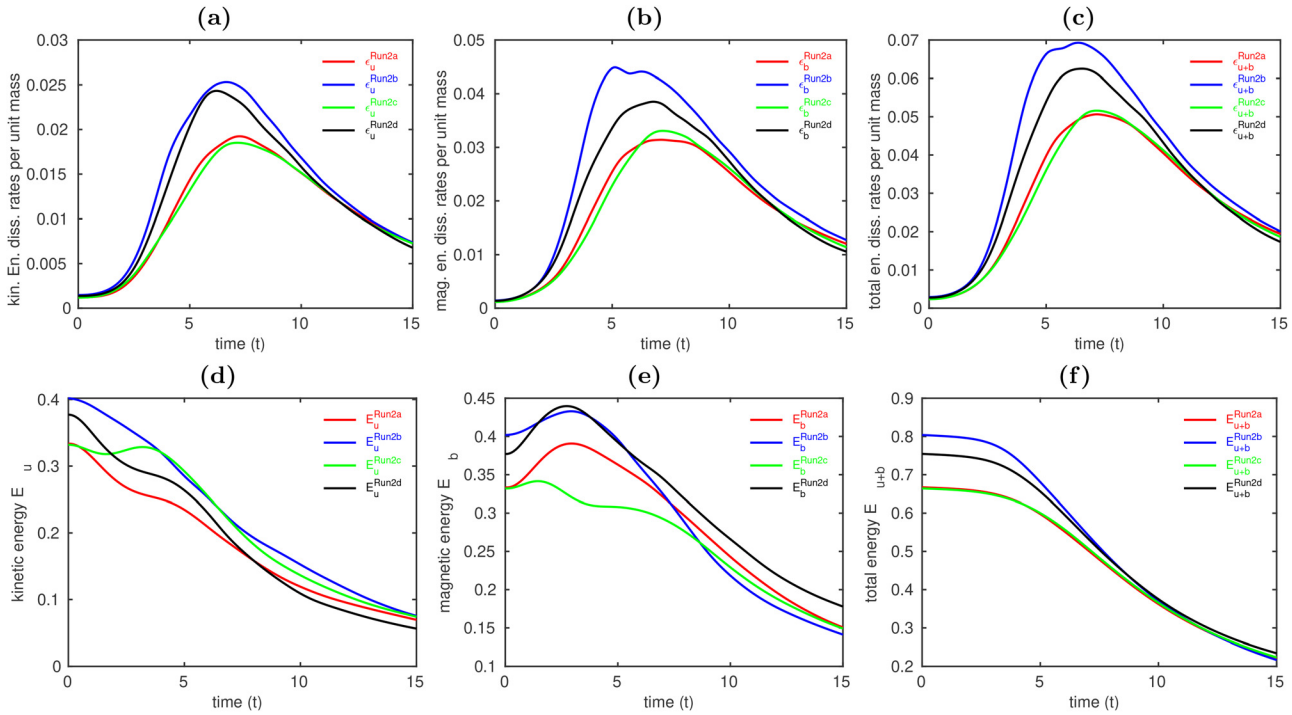

FIG. 4. Plots vs time t of (a) the kinetic-energy dissipation rate ϵ_u, (b) the magnetic-energy dissipation rate ϵ_b, (c) the total-energy dissipation rate ϵ; (d) the kinetic energy E_u, (e) magnetic energy E_b, and (f) the total energy E for Run2a (red-solid curves), Run2b (blue-solid curves), Run2c (green-solid curves), and Run2d (black-solid curves).

In all these PDFs, there are, roughly speaking, two peaks at $\cos\theta \simeq \pm 1$, which quantify the degree of antialignment ($\theta = 180°$) and alignment ($\theta = 0°$) between the two vectors. The amplitudes of these peaks depend upon the parameters in our DNSs. One qualitative trend shows up clearly: the alignment and antialignment and peaks [Figs. 6(a) and 7(a) for the pair $\{\mathbf{u}, \mathbf{b}\}$] are more pronounced in the 3D MHD runs (Run3 and Run5a) than in their 3D HMHD counterparts, and this trend of the suppression of the peaks appears in most of the PDFs we show in Figs. 6 and 7. In 3D MHD, the alignment or antialignment of $\{\mathbf{u}, \mathbf{b}\}$ is associated with a *depletion of nonlinearity*. This can be seen most simply by writing the 3D MHD equations in terms of Elsässer variables.[9] To the extent that the alignment or antialignment of peaks in the PDF of the cosine of the angle between $\{\mathbf{u}, \mathbf{b}\}$ are suppressed in 3D HMHD, relative to 3D MHD, we conclude that this depletion of nonlinearity is also suppressed.

We remark that the PDFs of the cosines of the angles mentioned above are related to PDFs of various helicities, which we list below:

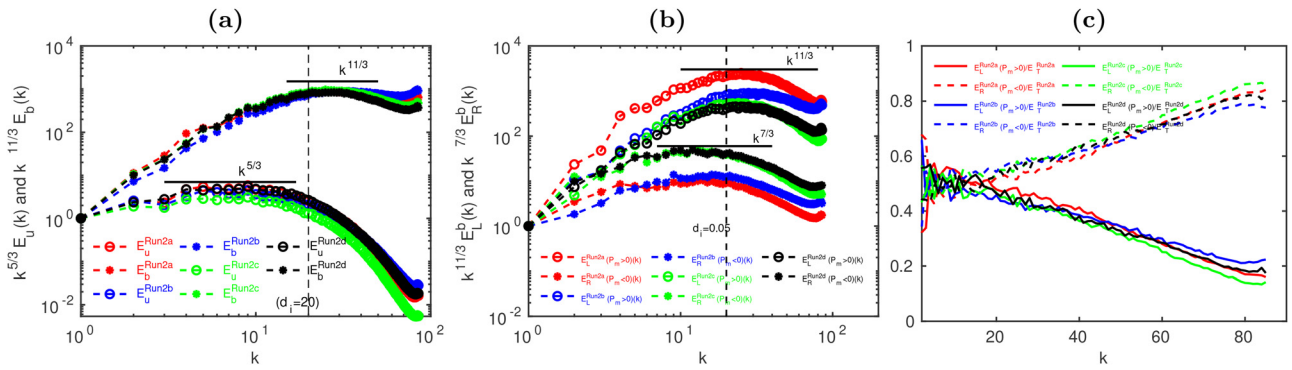

FIG. 5. Log–log (base 10) plots vs the wave number k of: (a) the compensated kinetic energy spectra $k^{5/3}E_u(k)$ (lower curves) and the compensated magnetic energy spectra $k^{11/3}E_b(k)$ (upper curves) from Run2a (red), Run2b (blue), Run2c (green), and Run2d (black); and (b) log–log (base 10) plots of the compensated magnetic energy spectra for the fluctuations $P_m \geq 0$ and $P_m \leq 0$ from the same runs. (c) Plots vs k of the energy ratios E_L/E_T and E_R/E_T from the same runs.

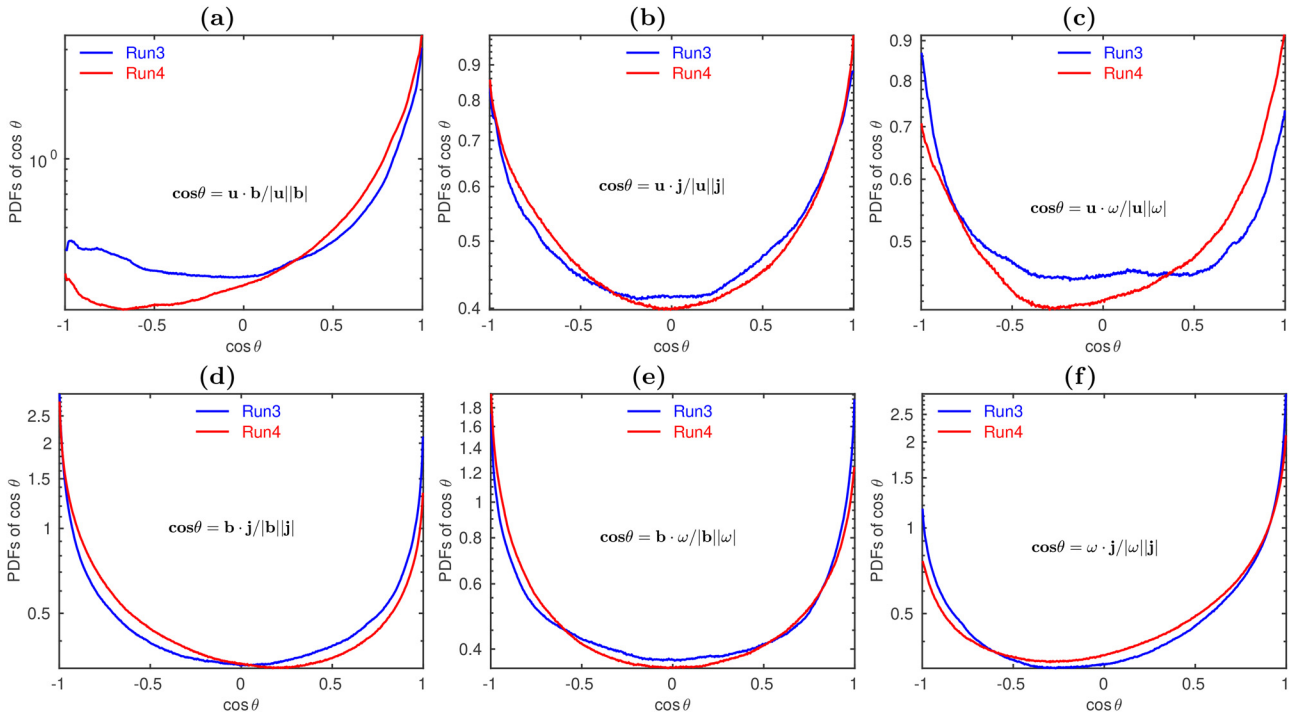

FIG. 6. Semilog (base 10) plots of PDFs of cosines of angles, denoted by θ, between (a) **u** and **b**, (b) **u** and **j**, (c) **u** and $\boldsymbol{\omega}$, (d) **b** and **j**, (e) **b** and $\boldsymbol{\omega}$, and (f) $\boldsymbol{\omega}$ and **j** from Run3 (blue curves) and Run4 (red curves).

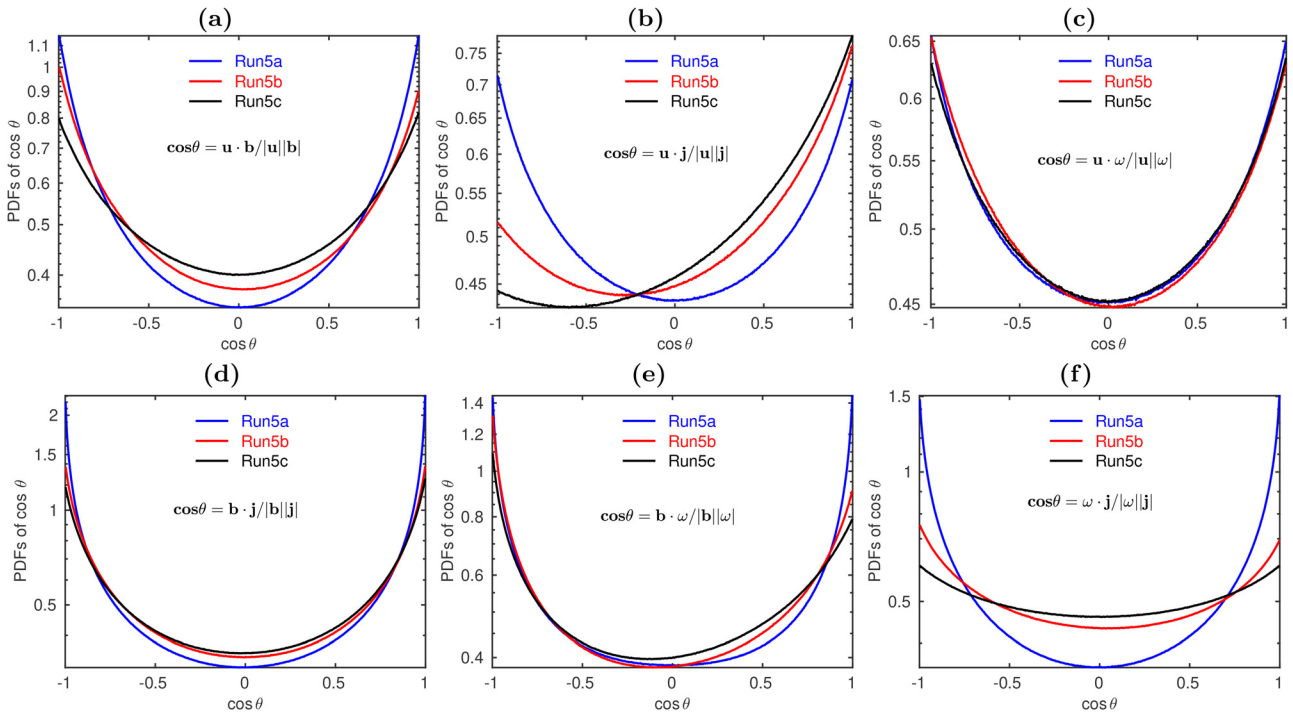

FIG. 7. Semilog (base 10) plots of PDFs of cosines of angles, denoted by θ, between (a) **u** and **b**, (b) **u** and **j**, (c) **u** and $\boldsymbol{\omega}$, (d) **b** and **j**, (e) **b** and $\boldsymbol{\omega}$, and (f) $\boldsymbol{\omega}$ and **j** from Run5a (blue curves), Run5b (red curves), and Run5c (black curves).

$$\begin{aligned} H_c &= \langle \mathbf{u} \cdot \mathbf{b} \rangle; \\ H_m &= \langle \mathbf{A} \cdot \mathbf{b} \rangle; \\ H_u &= \langle \mathbf{u} \cdot \boldsymbol{\omega} \rangle; \\ H_g &= H_m + 2d_i H_c + d_i^2 H_u. \end{aligned} \tag{18}$$

Here, H_c is the cross helicity; H_m is the magnetic helicity, with $\mathbf{A}$ the vector potential that follows from $\mathbf{b} = \nabla \times \mathbf{A}$; H_u is the kinetic helicity; and H_g is a generalized helicity that is useful in 3D HMHD. H_u is conserved for an ideal, unforced fluid; in the absence of forcing, H_m is conserved in both ideal 3D MHD and ideal 3D HMHD; H_c is conserved in ideal, unforced 3D MHD, but not in its 3D HMHD counterpart; in ideal, unforced 3D HMHD, the generalized cross helicity H_g is conserved.[71]

It is useful to define the electron velocity $\mathbf{v_e} \equiv \mathbf{u} - d_i \nabla \times \mathbf{b}$.[29] In Figs. 8(a) and 8(b), we present, respectively, the PDFs of the cosines of the angles between (a) $\mathbf{v_e}$ and $\mathbf{j}$ and (b) $\mathbf{v_e}$ and $\mathbf{b}$ from runs Run5a (blue curve), Run5b (red curve), and Run5c (black curve). In Figs. 8(c) and 8(d), we present similar plots for Run3 (blue curve) and Run4 (red curve).

C. Joint probability distribution functions

Insights into the topology of the flows can also be obtained by studying joint PDFs (JPDFs) of invariants of the velocity-gradient tensor and the moduli of the vorticity and the current as has been done in 3D MHD turbulence.[8] We obtain such JPDFs for 3D HMHD and compare them with their MHD counterparts.

We display color-contour plots of the joint probability distribution functions (JPDFs) of Q and R, at the cascade-completion time τ_c, in Fig. 9 from Run3, Run4, Run5a, and Run5c, with Q and R the following, well-known invariants (see, e.g., Ref. 8) for an ideal, incompressible fluid:

$$\begin{aligned} Q &= -\frac{1}{2} tr(A^2); \\ R &= -\frac{1}{3} tr(A^3); \end{aligned} \tag{19}$$

here, A is the velocity-derivative tensor with components $A_{ij} = \partial_i u_j$; the zero-discriminant line $D = \frac{27}{4} R^2 + Q^3 = 0$ is shown by black curves in these plots. We observe that the characteristic, tear-drop shape of these JPDFS of Q and R is more prominent in 3D HMHD turbulence (Run4 and Run5c) than in their 3D MHD counterparts (Run3 and Run5a), and the tails of these JPDFs are more elongated in 3D HMHD turbulence (Run4 and Run5c) than in their 3D MHD counterparts (Run3 and Run5a).

In Fig. 10, we show plots of JPDFs of ω and j, the moduli of the vorticity ($\boldsymbol{\omega}$), and the current ($\mathbf{j}$), at the cascade-completion time τ_c

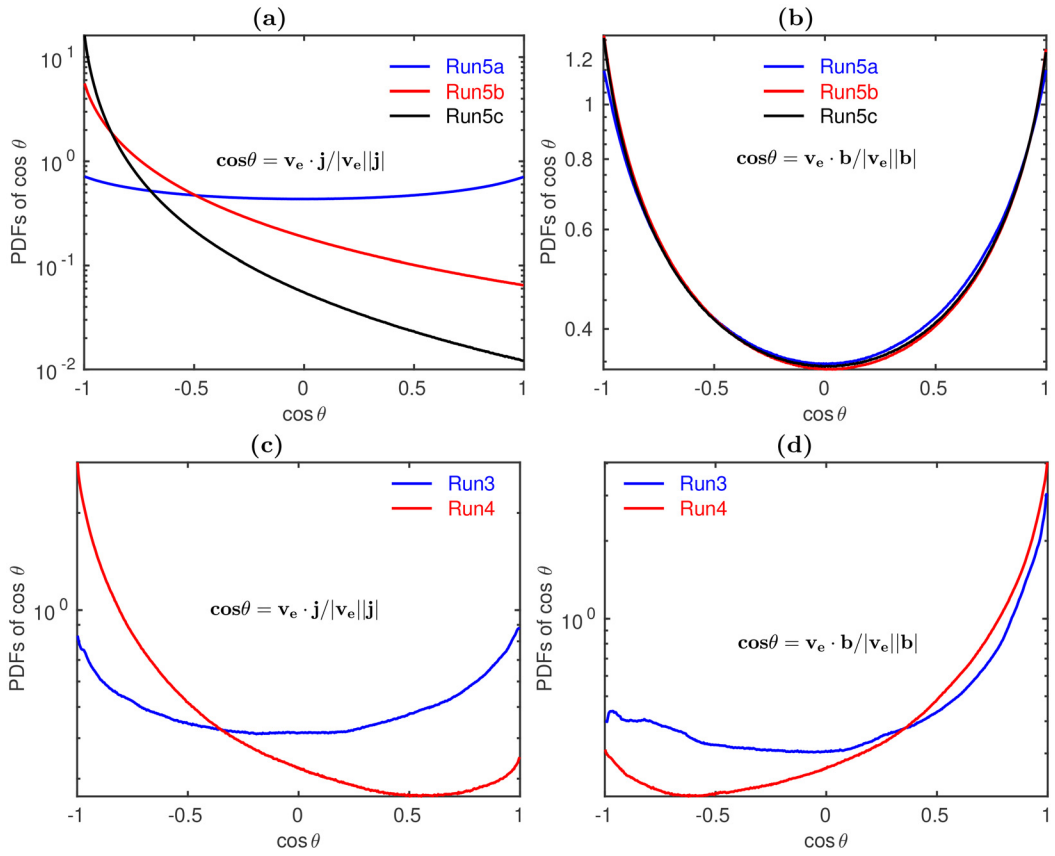

FIG. 8. Semilog (base 10) plots of PDFs of cosines of angles, denoted by θ, between (a) $\mathbf{v}_e$ and $\mathbf{j}$, and (b) $\mathbf{v}_e$ and $\mathbf{b}$ from Run5a (blue curves), Run5b (red curves), and Run5c (black curves); (c) and (*d*) are similar plots from Run3 (blue curves) and Run4 (red curves).

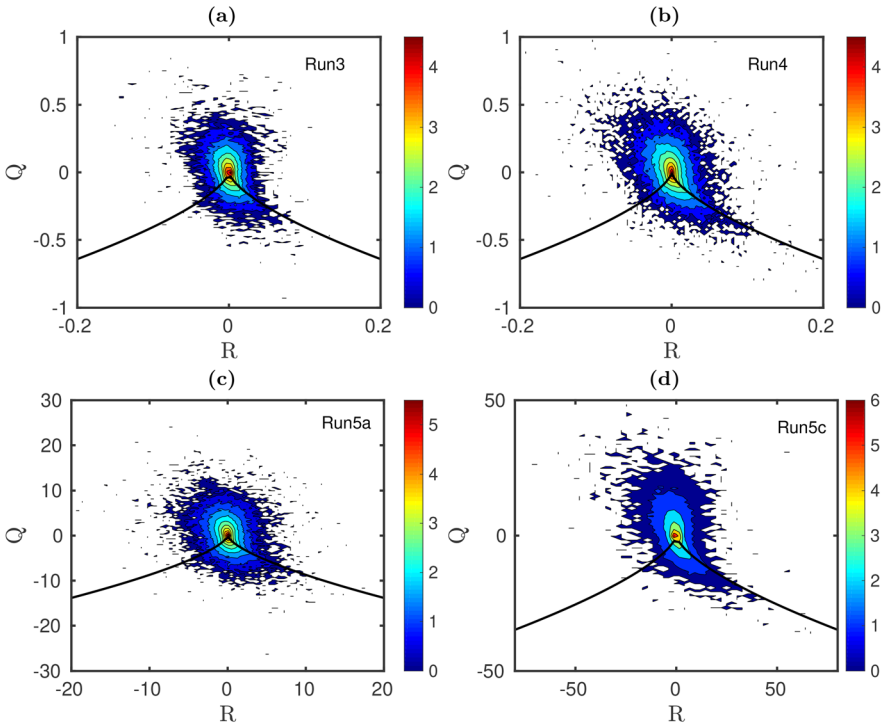

FIG. 9. Color-contour plots of the JPDFs of Q and R for (a) Run3, (b) Run4, (c) Run5a, and (d) Run5c.

from Run3, Run4, Run5a, and Run5c. We observe that in 3D MHD turbulence (Run3 and Run5a), the outer region of the JPDFs of ω and j shows curved, roughly circular contours, whereas in 3D HMHD turbulence (Run4 and Run5c), the counterparts of these contours are flattened and suppressed significantly; furthermore, there is an elongation of the JPDFs of ω and j along the axes, at low values of ω and j. Similar observations of the JPDFs of ω and j have been reported in Ref. 72.

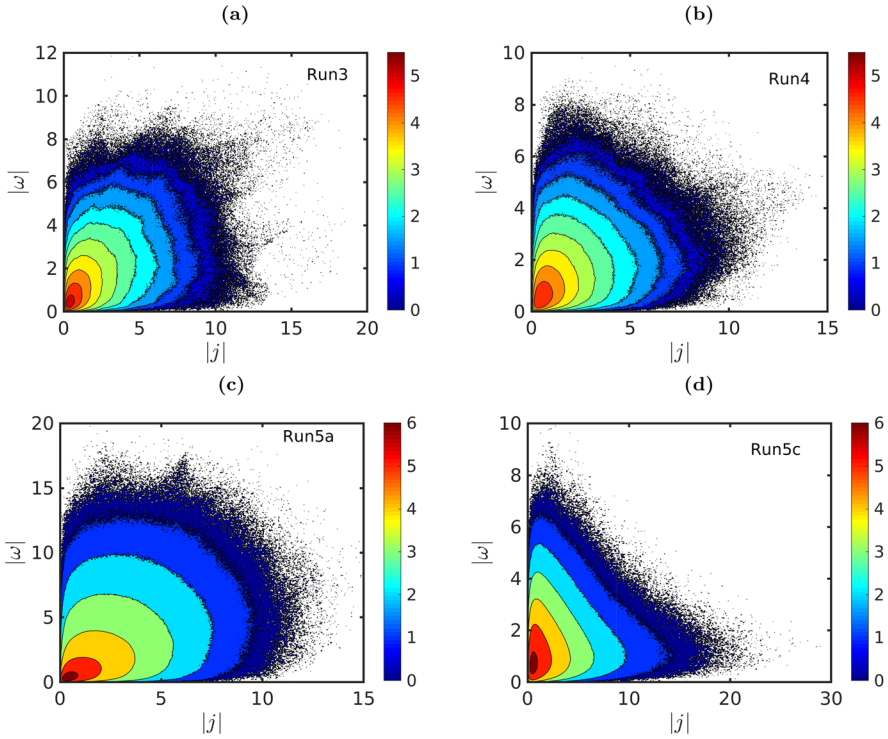

FIG. 10. Color-contour plots of the JPDFs of ω and j for (a) Run3, (b) Run4, (c) Run5a, and (d) Run5c.

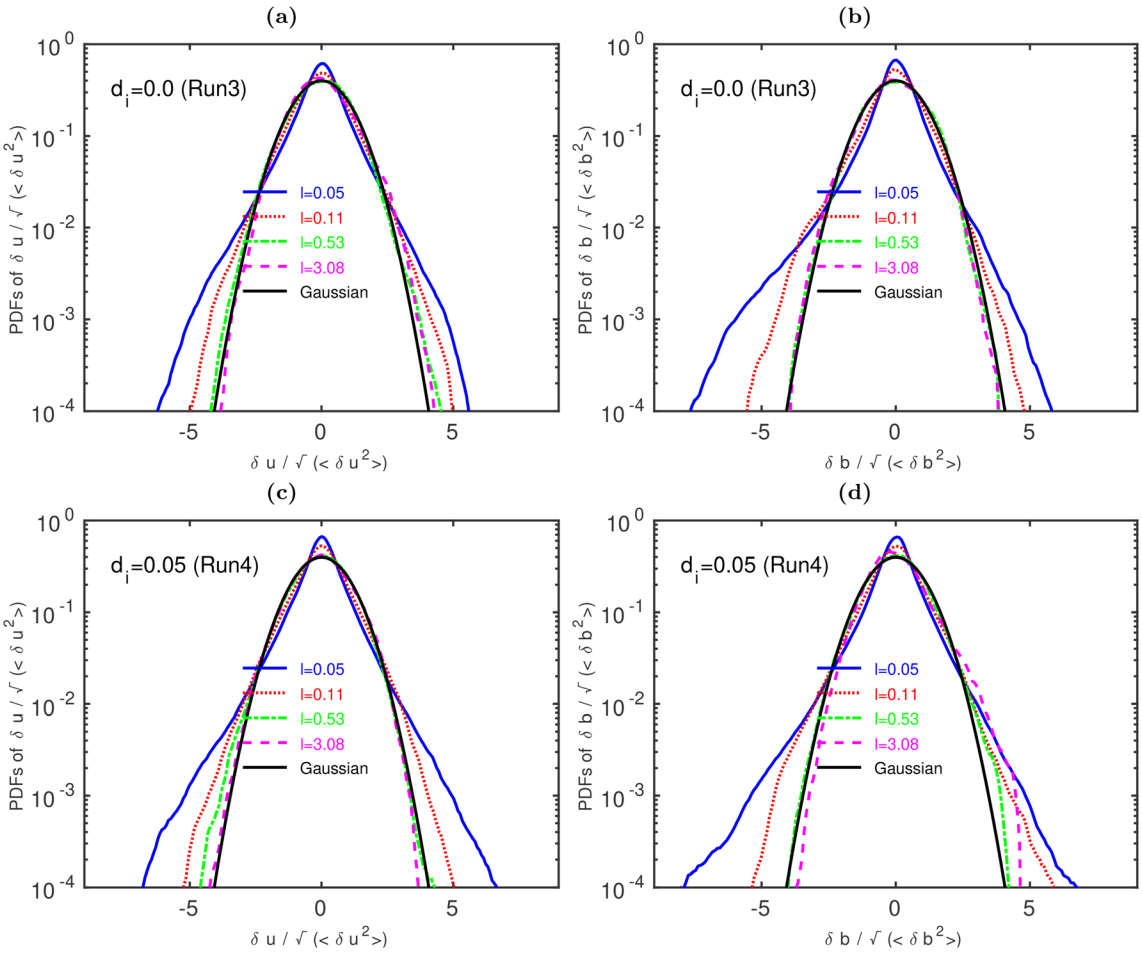

FIG. 11. Semilog (base 10) plots of PDFs of (a) the velocity- and (b) magnetic-field increments from Run3 for $l = 0.05$ (blue solid lines), 0.11 (red dotted lines), 0.53 (green dashed-dotted lines), and 3.08 (magenta dashed lines). (c) and (d) are the corresponding plots from Run4; for reference, we also show zero-mean and unit-variance Gaussian PDFs (black lines) in each subplots.

D. Intermittency

At the cascade-completion time τ_c, we investigate intermittency in 3D HMHD turbulence, and in its 3D MHD counterpart, by calculating the length-scale-l dependence of (a) PDFs of the velocity and magnetic-field increments [Eq. (11)] and (b) of the velocity and magnetic-field structure functions [Eq. (11)] and, therefrom, their order-p multiscaling exponents, Eqs. (12) and (13), in the inertial and the second-inertial ranges. We also examine the dependence on l of the hyperflatness Eq. (14).

In Figs. 11 and 12, we display the l dependence of the PDFs of, respectively, the velocity- and magnetic-field increments, from Run3, Run4, Run5a, Run5b, and Run5c. In these PDFs, l goes from the second-inertial range to the inertial range: $l = 0.05$ (blue solid curves), $l = 0.11$ (red dotted curves), $l = 0.53$ (green dashed-dotted curves), and $l = 3.08$ (magenta dashed curves) from Run3 and Run4; we give similar plots for Run5a–Run5c in Fig. 12; we include, for reference, Gaussian PDFs (black lines) with zero mean and unit variance. We note that the field-increment PDFs show tails that deviate significantly from those of Gaussian PDFs: the smaller the value of l, the greater this deviation, a clear signature of small-scale intermittency (see, e.g., Ref. 73).

In Figs. 13(a) and 13(b), we present semilog plots of PDFs of magnetic-field increments from simulations Run5a (MHD) and Run5c (HMHD) for many values of l in the range $l = 0.11$ to $l = 0.53$, which include length scales in the second-inertial range for the HMHD run; in these units, $d_i = 0.05 \times 2.0\pi \simeq 0.314$. The tails of these PDFs show considerable deviations from a Gaussian PDF, which is shown for comparison.

We turn now to structure functions [Eq. (11)], multiscaling exponents [Eqs. (12) and (13)], and the ratios of these exponents. We present plots of such structure functions in Figs. 14–18. To extract multiscaling exponents [Eqs. (12) and (13)] directly, we use log–log (base 10) plots of structure functions [Eq. (11)] vs the separation l. We obtain such plots, at t_c, for Run3 and Run4 in, respectively, Figs. 14(a), 14(b), 15(a), and 15(b), for order p from 1 to 6; we indicate by straight, black lines the regions that we use to obtain estimates for the

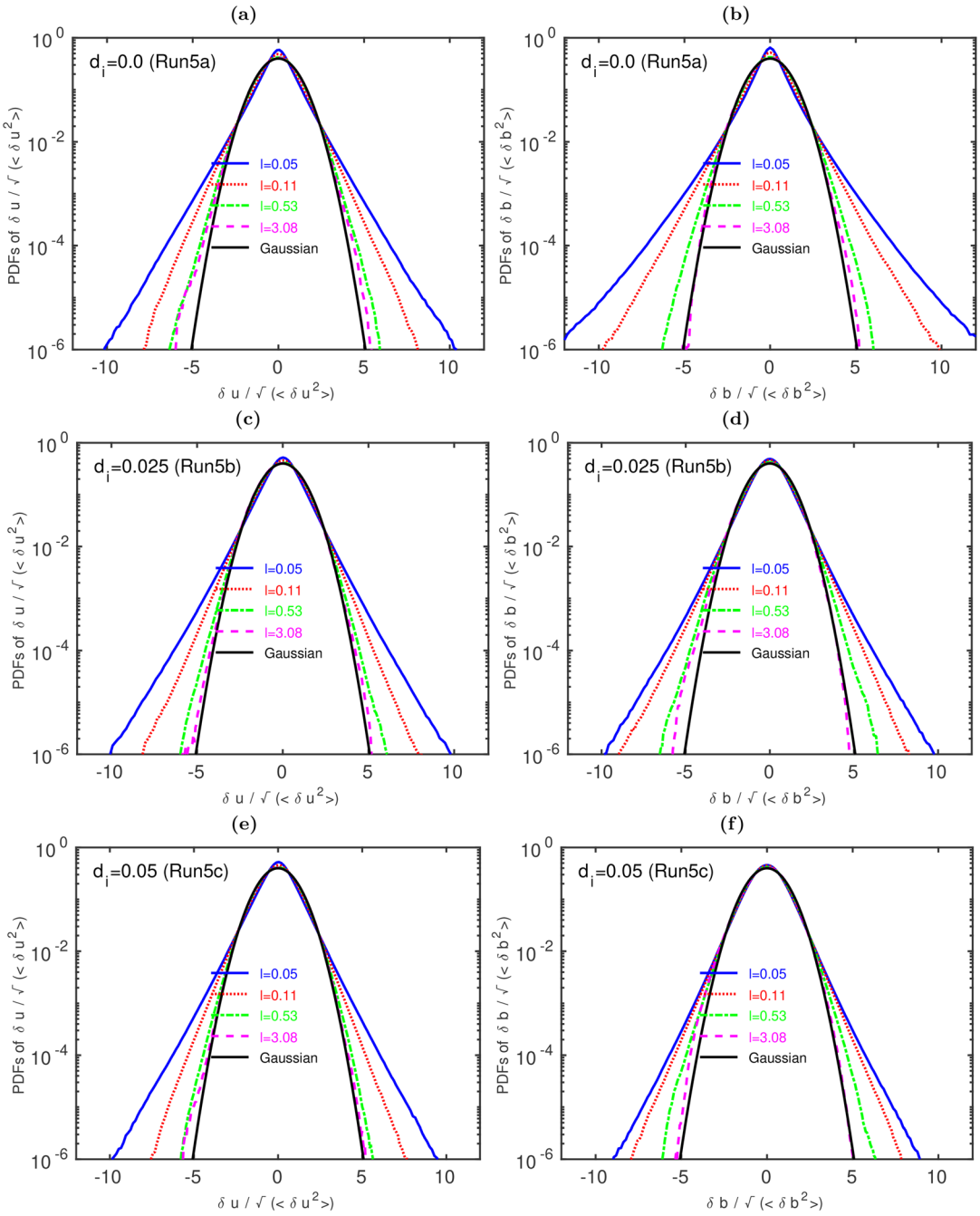

FIG. 12. Semilog (base 10) plots of PDFs of (a) the velocity- and (b) magnetic-field increments from Run5a for $l = 0.05$ (blue solid lines), 0.11 (red dotted lines), 0.53 (green dashed-dotted lines), and 3.08 (magenta dashed lines). The corresponding plots from Run5b and Run5c are shown in (c)–(f), respectively; for reference, we also show zero-mean and unit-variance Gaussian PDFs (black lines).

multiscaling exponents [Eqs. (12) and (13)]; we get these exponents and their error bars by using a local-slope analysis.[8] We present plots, vs p, of the resulting multiscaling exponents [Eqs. (12) and (13)], for Run3 and Run4 in, respectively, Figs. 14(c), 15(c), and 15(d). If the scaling range extends over a limited range of scales, this range can often be extended by using the extended-self-similarity (ESS) procedure.[74,75] In this procedure, we use log–log (base 10) plots of the structure function of order p, vs, e.g., the $p = 3$ structure function;

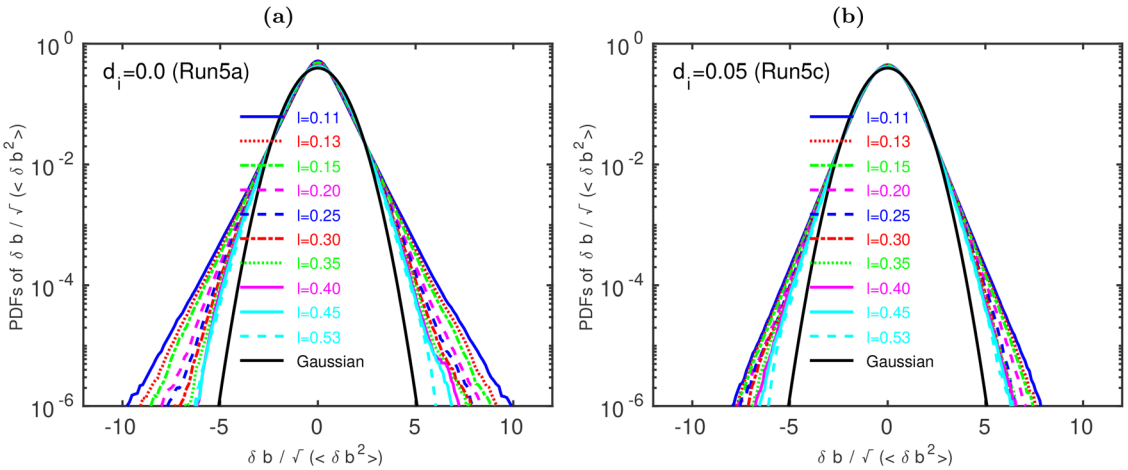

FIG. 13. Semilog plots (base 10) of PDFs of magnetic-field increments from simulations (a) Run5a (MHD) and (b) Run5c (HMHD) for many values of l in the range $l = 0.11$ to $l = 0.53$, which include length scales in the second inertial range for the HMHD run; in these units, $d_i = 0.05 \times 2.0\pi \simeq 0.314$. The tails of these PDFs show considerable deviations from a Gaussian PDF, which is shown for comparison (via black lines).

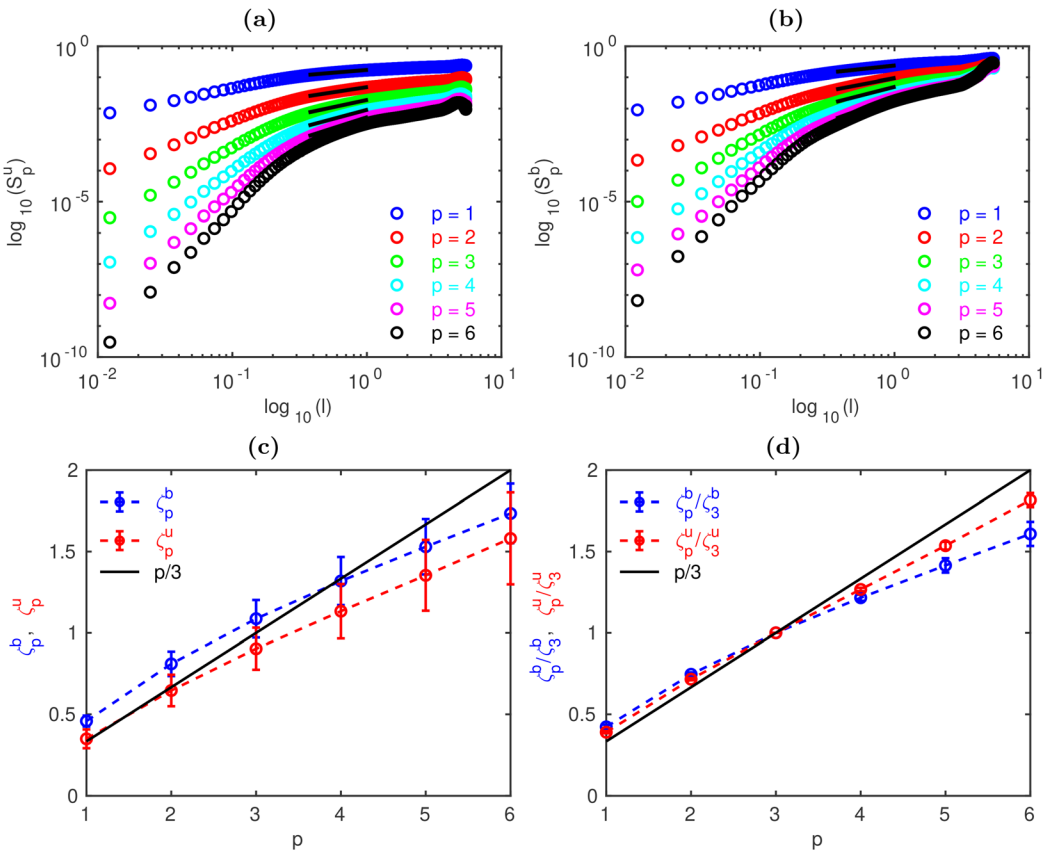

FIG. 14. Log–log (base 10) plots vs l, at t_c, for *Run3* and (a) velocity and (b) magnetic structure functions [Eq. (11)]; the order p goes from 1 to 6; we indicate by straight, black lines the regions that we use to obtain estimates for the multiscaling exponents [Eqs. (12) and (13)]. Plots vs the order p of (c) the multiscaling exponents [Eqs. (12) and (13)] and (d) their ratios; for reference, we show the linear K41 scaling of exponents with $p/3$.

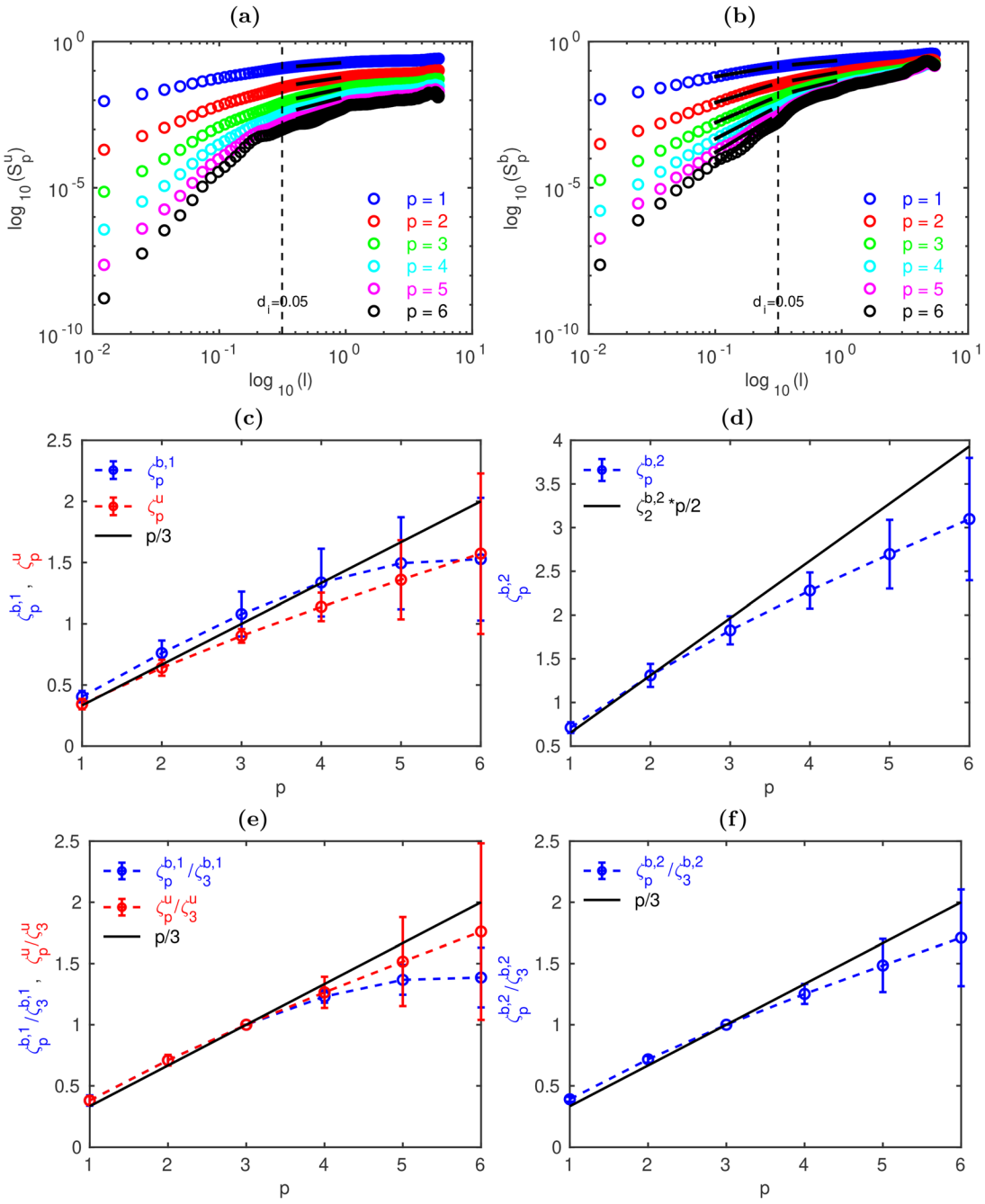

FIG. 15. Log–log (base 10) plots vs l, at t_c, for Run4 and (a) velocity and (b) magnetic structure functions [Eq. (11)]; the order p goes from 1 to 6; we indicate by straight, black lines the regions that we use to obtain estimates for the multiscaling exponents [Eqs. (12) and (13)]. Plots vs the order p of the multiscaling exponents [Eqs. (12) and (13)] for (c) the inertial range and (d) the second-inertial range. Plots vs the order p of the ratios of multiscaling exponents [Eqs. (12) and (13)] for (e) the inertial range and (f) the second-inertial range; for reference, we show simple scaling predictions.

straight-line regions in such plots yield the ratios of the order p and order $p=3$ multiscaling exponents [Eqs. (12) and (13)]. [This has proved to be especially useful in incompressible-fluid turbulence, where the third-order exponent is known to be 1.] We give such ESS plots for structure functions in Figs. 16(a) and 16(b) (Run5a), 17(a) and 17(b) (Run5b), and 18(a) and 18(b) (Run5c); we then plot the resulting multiscaling exponent [Eqs. (12) and (13)] ratios in Figs. 15(e) and 15(f) (Run4), 16(c) (Run5a), 17(c) and 17(d) (Run5b),

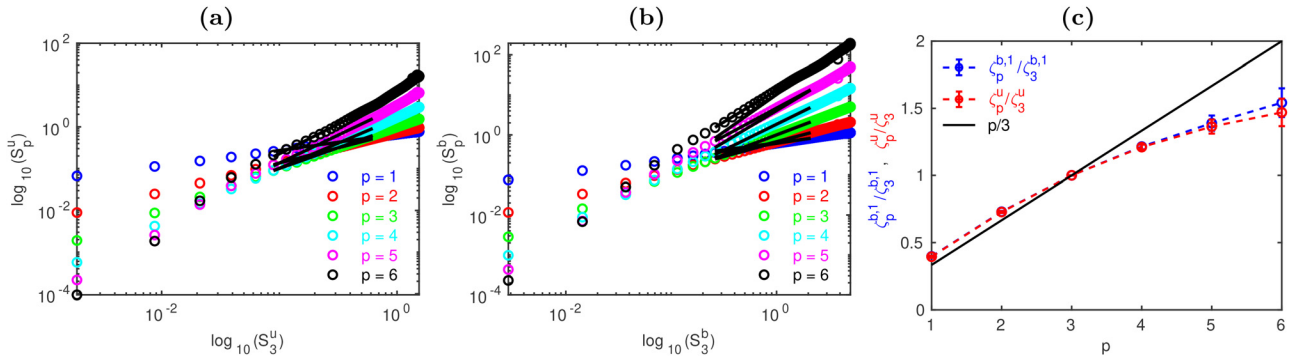

FIG. 16. Log–log (base 10) ESS plots (see the text), at t_c, for Run5a and (a) velocity and (b) magnetic structure functions [Eq. (11)]; the order p goes from 1 to 6; we indicate by straight, black lines the regions that we use to obtain estimates for the ratios of multiscaling exponents [Eqs. (12) and (13)]. Plots vs the order p of (c) the ratios of multiscaling exponents [Eqs. (12) and (13)]; for reference, we show the K41 scaling of exponents with $p/3$.

and 18(c) and 18(d) (Run5c). We list our values for multiscaling exponents [Eqs. (12) and (13)], along with error bars, in Tables II–IV; these Tables provide a quantitative summary of our results for these exponents. We note, at the qualitative level, that prior experimental studies[54] suggest that the magnetic-field structure functions in 3D HMHD turbulence exhibit (a) *inertial* and *second-inertial* scaling regions and (b) multiscaling is replaced by simple scaling in the second of these ranges; our results are in consonance with these observations.

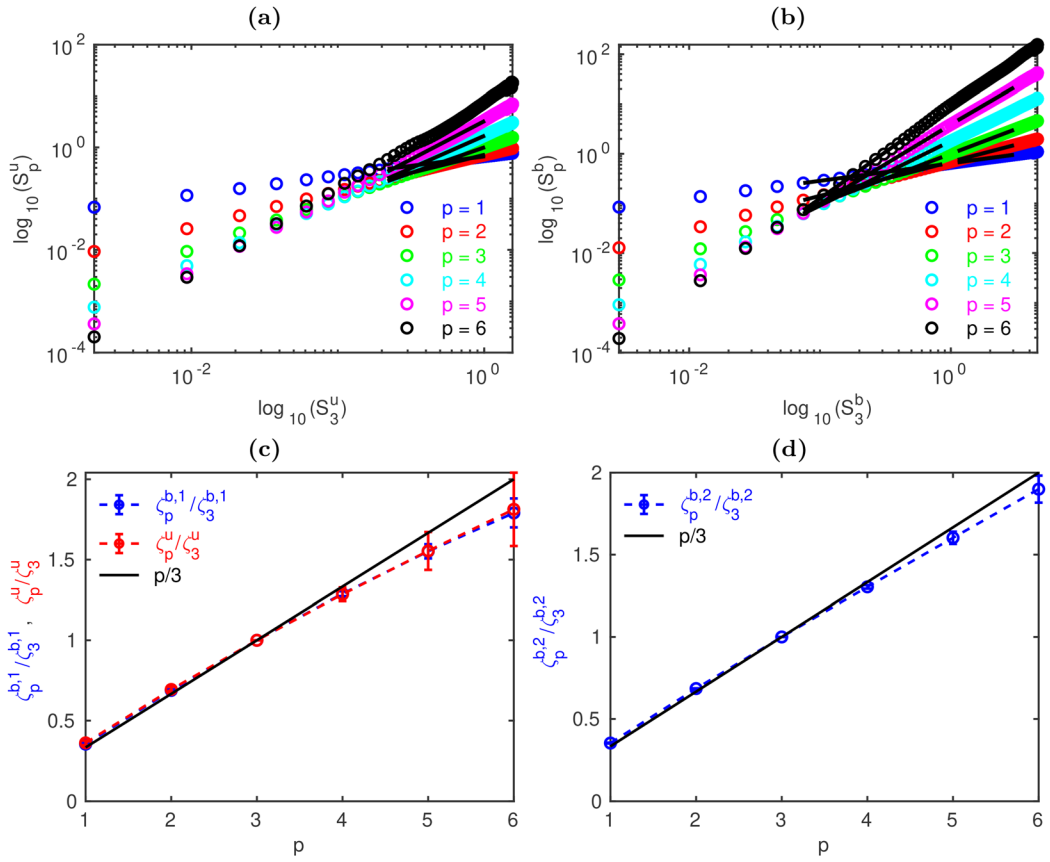

FIG. 17. Log–log (base 10) ESS plots (see the text), at t_c, for Run5b and (a) velocity and (b) magnetic structure functions [Eq. (11)]; the order p goes from 1 to 6; we indicate by straight, black lines the regions that we use to obtain estimates for the ratios of multiscaling exponents [Eqs. (12) and (13)]. Plots vs the order p of the ratios of multiscaling exponents [Eqs. (12) and (13)] for (c) the inertial range and (d) the second-inertial range; for reference, we show the K41 scaling of exponents with $p/3$.

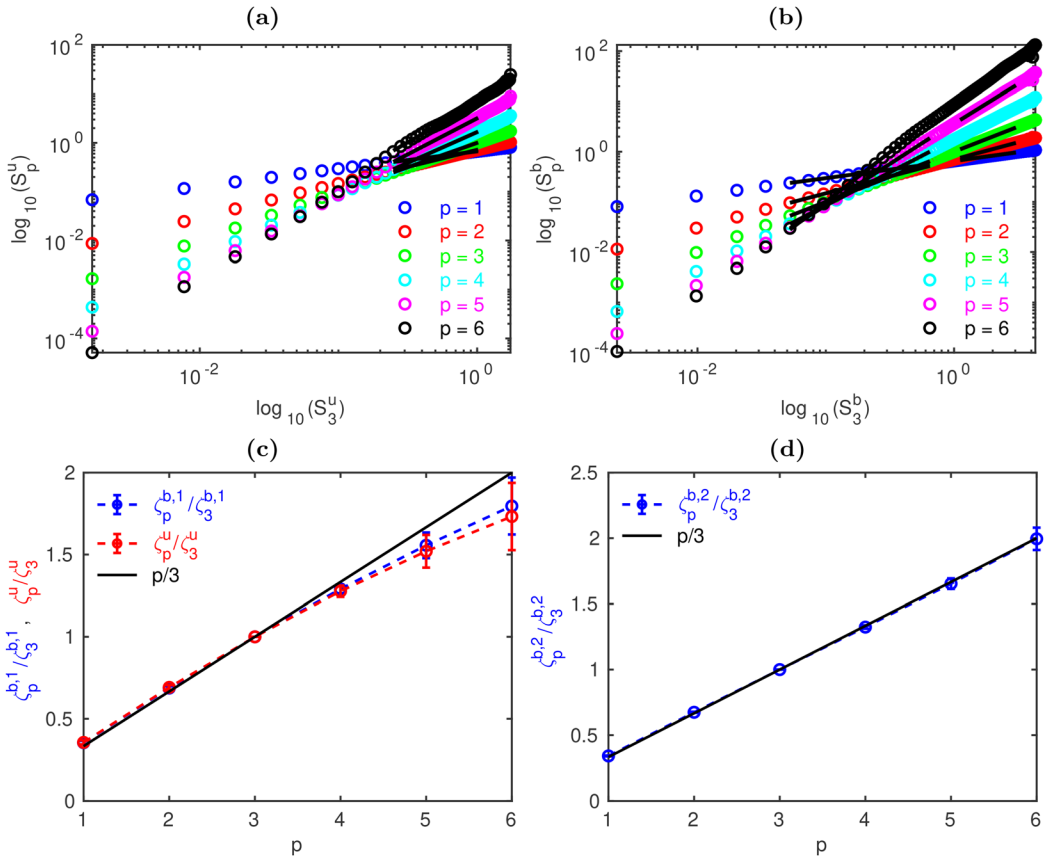

FIG. 18. Log–log (base 10) ESS plots (see the text), at t_c, for Run5c and (a) velocity and (b) magnetic structure functions [Eq. (11)]; the order p goes from 1 to 6; we indicate by straight, black lines the regions that we use to obtain estimates for the ratios of multiscaling exponents [Eqs. (12) and (13)]. Plots vs the order p of the ratios of multiscaling exponents [Eqs. (12) and (13)] for (c) the inertial range and (d) the second-inertial range; for reference, we show the K41 scaling of exponents with $p/3$.

The length-scale dependence of the hyperflatness [Eq. (14)] is often used to characterize small-scale intermittency. We present semi-log plots of the hyperflatnesses [Eq. (14)], for the velocity and the magnetic fields, in Run5a–Run5c [Figs. 19(a)–19(c)], respectively. In these plots, we observe that these hyperflatnesses are more-or-less flat, over a large range of l, but they increase rapidly, at small l; this is the hallmark of small-scale intermittency.

IV. CONCLUSIONS

Our study, which has been motivated by the uncertainties in spectral exponents and the statistical properties of 3D HMHD turbulence, is a systematic investigation of these properties by pseudospectral DNSs. Although many numerical studies of 3D HMHD turbulence have been carried out earlier, none of them has compared results from two different types of initial conditions {initial condition

TABLE II. List of the multiscaling exponents [Eqs. (12) and (13)], for Run3 and Run4. Run4 has two sets of exponents, one for the inertial range and the other for the second-inertial range (see the text).

P	$\zeta_p^{u,Run3}$	$\zeta_p^{b,Run3}$	$\zeta_p^{u,Run4}$	$\zeta_p^{(b,1),Run4}$	$\zeta_p^{(b,2),Run4}$
1	0.35 ± 0.06	0.45 ± 0.03	0.34 ± 0.04	0.40 ± 0.04	0.71 ± 0.06
2	0.65 ± 0.10	0.81 ± 0.07	0.64 ± 0.07	0.76 ± 0.10	1.31 ± 0.13
3	0.90 ± 0.13	1.09 ± 0.12	0.90 ± 0.06	1.08 ± 0.18	1.83 ± 0.16
4	1.13 ± 0.17	1.32 ± 0.15	1.14 ± 0.12	1.34 ± 0.28	2.28 ± 0.21
5	1.35 ± 0.22	1.53 ± 0.17	1.36 ± 0.32	1.49 ± 0.38	2.69 ± 0.39
6	1.58 ± 0.28	1.73 ± 0.18	1.57 ± 0.66	1.53 ± 0.50	3.10 ± 0.70

TABLE III. List of the ratios of multiscaling exponents [Eqs. (12) and (13)], for Run3 and Run4. Run4 has two sets of exponents, one for the inertial range and the other for the second-inertial range (see the text).

p	$(\zeta_p^u/\zeta_3^u)^{Run3}$	$(\zeta_p^b/\zeta_3^b)^{Run3}$	$(\zeta_p^u/\zeta_3^u)^{Run4}$	$(\zeta_p^{b,1}/\zeta_3^{b,1})^{Run4}$	$(\zeta_p^{b,2}/\zeta_3^{b,2})^{Run4}$
1	0.39 ± 0.01	0.42 ± 0.01	0.38 ± 0.03	0.38 ± 0.04	0.39 ± 0.02
2	0.72 ± 0.01	0.75 ± 0.01	0.71 ± 0.04	0.71 ± 0.04	0.72 ± 0.03
3	1.0 ± 0.00	1.0 ± 0.00	1.0 ± 0.00	1.0 ± 0.00	1.0 ± 0.00
4	1.27 ± 0.01	1.22 ± 0.02	1.26 ± 0.13	1.23 ± 0.05	1.25 ± 0.08
5	1.54 ± 0.02	1.42 ± 0.04	1.52 ± 0.36	1.37 ± 0.12	1.48 ± 0.22
6	1.82 ± 0.04	1.61 ± 0.07	1.76 ± 0.72	1.39 ± 0.24	1.71 ± 0.39

TABLE IV. List of the ratios of multiscaling exponents [Eqs. (12) and (13)], obtained via the ESS procedure (see the text), for Run5a, Run5b, and Run5c. Run5b and Run5c have two sets of exponents, one for the inertial range and the other for the second-inertial range (see the text).

p	$(\zeta_p^u/\zeta_3^u)^{Run5a}$	$(\zeta_p^b/\zeta_3^b)^{Run5a}$	$(\zeta_p^u/\zeta_3^u)^{Run5b}$	$(\zeta_p^{b,1}/\zeta_3^{b,1})^{Run5b}$	$(\zeta_p^{b,2}/\zeta_3^{b,2})^{Run5b}$	$(\zeta_p^u/\zeta_3^u)^{Run5c}$	$(\zeta_p^{b,1}/\zeta_3^{b,1})^{Run5c}$	$(\zeta_p^{b,2}/\zeta_3^{b,2})^{Run5c}$
1	0.39 ± 0.01	0.40 ± 0.01	0.36 ± 0.01	0.35 ± 0.01	0.35 ± 0.01	0.36 ± 0.01	0.35 ± 0.01	0.34 ± 0.01
2	0.73 ± 0.01	0.73 ± 0.01	0.70 ± 0.02	0.69 ± 0.01	0.68 ± 0.01	0.69 ± 0.01	0.69 ± 0.01	0.67 ± 0.01
3	1.0 ± 0.00	1.0 ± 0.00	1.0 ± 0.00	1.0 ± 0.00	1.0 ± 0.00	1.0 ± 0.00	1.0 ± 0.00	1.0 ± 0.00
4	1.21 ± 0.02	1.21 ± 0.02	1.28 ± 0.04	1.29 ± 0.02	1.30 ± 0.01	1.28 ± 0.03	1.29 ± 0.03	1.32 ± 0.01
5	1.36 ± 0.05	1.39 ± 0.06	1.55 ± 0.12	1.55 ± 0.04	1.60 ± 0.04	1.52 ± 0.10	1.56 ± 0.08	1.65 ± 0.04
6	1.47 ± 0.10	1.54 ± 0.11	1.81 ± 0.23	1.79 ± 0.09	1.89 ± 0.08	1.73 ± 0.20	1.80 ± 0.17	1.99 ± 0.09

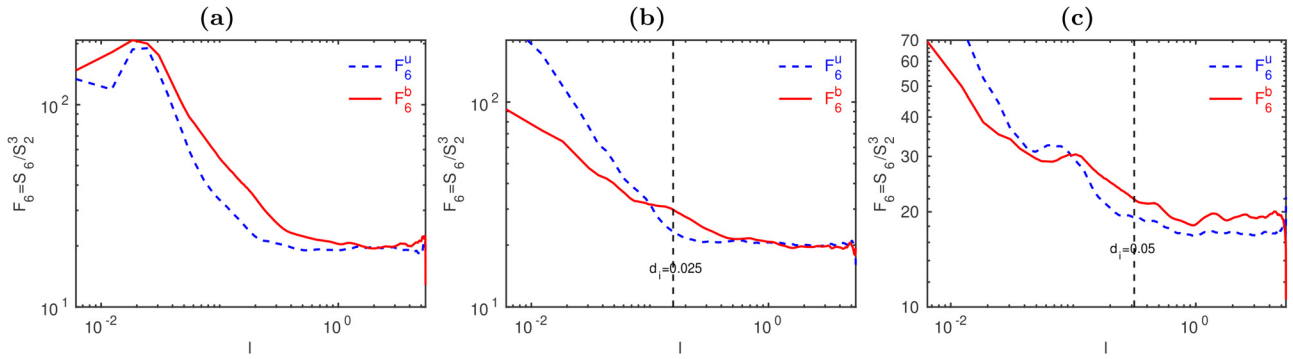

FIG. 19. Log–log (base 10) plots of the hyperflatnesses [Eq. (14)], for the velocity and the magnetic fields, in (a) Run5a, (b) Run5b, and (c) Run5c.

A [Eq. (8) and Run2–Run4] and initial condition B [Eq. (9) and Run5b and Run5c]} nor studied, in one work, the different statistical properties we consider. (For similar studies of 3D MHD turbulence, we refer the reader to Refs. 8 and 70). Our work provides valuable insights into the initial-condition dependence of the spectral exponent α_1 and the multiscaling exponents [Eqs. (12) and (13)]. We find clear evidence of inertial- and second-inertial range scaling, with the value of the spectral exponent α consistent with the K41 result 5/3. In the second-inertial range, the value of α_1 is consistent with (A) 11/3, for the initial condition A, and (B) 7/3, for the initial condition B. These different values can be attributed, in part, to the disparities in the k dependence of $E_b(k)/E_u(k)$ for these two initial conditions. Our computations of the PDFs of the cosines of the angles between various fields, such as the velocity **u** and $\boldsymbol{\omega}$ or **b** and **j**, help us highlight the importance of the Hall term in suppressing the tendency of alignment (or antialignment) of these fields for both the initial conditions (A) and (B). We carry out a careful exploration of intermittency in 3D HMHD turbulence by calculating the PDFs of the velocity and magnetic-field increments as a function of the separation length scale l. We compute the l-dependence of velocity and magnetic-field structure functions and, therefrom, their order-p multiscaling exponents [Eqs. (12) and (13)]. In the inertial (second-inertial) range, we find clear signatures of multiscaling (simple scaling), in consonance with solar-wind results.[54]

In a future work, we will carry out the Hall-MHD analog of the studies of small-scale structures in MHD turbulence with the initial data of Refs. 65 and 66. Furthermore, it will be interesting to examine Hall-MHD flows by generalizing the studies in the following lattice Boltzmann models (LBM) papers on MHD flows that have appeared recently.[76,77]

ACKNOWLEDGMENTS

R.P. and S.K.Y. thank Nadia Bihari Padhan for discussions. S.K.Y. thanks the UGC-D.S. Kothari Postdoctoral Fellowship and Institute Research Grant (SVNIT); R.P. and S.K.Y. thank CSIR, National Supercomputing Mission (NSM), and SERB (India) for support and SERC (IISc) for computational resources. This research was partially supported by JSPS KAKENHI Grant Nos. 17K05734 and 20H00225, Japan. Many of the numerical simulations were performed on *Plasma Simulator* of NIFS with the support and under the auspices of the NIFS Collaboration Research program (NIFS20KNSSS133), as well as on the Oakforest-PACS supercomputer of the University of Tokyo, being partially supported by the Joint Usage/Research Center for Interdisciplinary Large-Scale Information Infrastructures in Japan (Grant Nos. jh190006-NAJ and jh200002-NAH).

AUTHOR DECLARATIONS

Conflict of Interest

The authors have no conflicts to disclose.

Author Contributions

Sharad K. Yadav: Conceptualization (equal), Formal analysis (equal), Writing – original draft (equal), and Writing – review & editing (equal). **Hideaki Miura:** Conceptualization (equal), Writing – original

draft (equal), and Writing – review & editing (equal). **Rahul Pandit:** Conceptualization (equal), Supervision (lead), Writing – original draft (equal), and Writing – review & editing (equal).

DATA AVAILABILITY

The data that support the findings of this study are available from the corresponding author upon reasonable request. Fortran scripts, e.g., for the standard calculation of energy spectra, can also be obtained from the corresponding author upon reasonable request.

REFERENCES

[1]A. R. Choudhuri, *The Physics of Fluids and Plasmas: An Introduction for Astrophysicists* (Cambridge University Press, 1998).
[2]V. Krishan, *Astrophysical Plasmas and Fluids* (Springer Science & Business Media, 1999), Vol. 235.
[3]G. Rüdiger and R. Hollerbach, *The Magnetic Universe: Geophysical and Astrophysical Dynamo Theory* (John Wiley & Sons, 2006).
[4]J. P. Goedbloed and S. Poedts, *Principles of Magnetohydrodynamics: With Applications to Laboratory and Astrophysical Plasmas* (Cambridge University Press, 2004).
[5]D. Biskamp, *Magnetohydrodynamic Turbulence* (Cambridge University Press, 2003).
[6]M. K. Verma, "Statistical theory of magnetohydrodynamic turbulence: Recent results," Phys. Rep. **401**, 229 (2004).
[7]P. A. Davidson, *An Introduction to Magnetohydrodynamics* (Cambridge University Press, 2002).
[8]G. Sahoo, P. Perlekar, and R. Pandit, "Systematics of the magnetic-Prandtl-number dependence of homogeneous, isotropic magnetohydrodynamic turbulence," New J. Phys. **13**, 013036 (2011).
[9]A. Basu, A. Naji, and R. Pandit, "Structure-function hierarchies and von Kármán–Howarth relations for turbulence in magnetohydrodynamical equations," Phys. Rev. E **89**, 012117 (2014).
[10]K. Moffatt and E. Dormy, *Self-Exciting Fluid Dynamos* (Cambridge University Press, 2019), Vol. 59.
[11]P. H. Roberts and G. A. Glatzmaier, "Geodynamo theory and simulations," Rev. Mod. Phys. **72**, 1081 (2000).
[12]W. L. Shew and D. P. Lathrop, "Liquid sodium model of geophysical core convection," Phys. Earth Planet. Inter. **153**, 136 (2005).
[13]R. Monchaux, M. Berhanu, M. Bourgoin, M. Moulin, P. Odier, J.-F. Pinton, R. Volk, S. Fauve, N. Mordant, F. Pétrélis *et al.*, "Generation of a magnetic field by dynamo action in a turbulent flow of liquid sodium," Phys. Rev. Lett. **98**, 044502 (2007).
[14]C. Salem, A. Mangeney, S. Bale, and P. Veltri, "Solar wind magnetohydrodynamics turbulence: Anomalous scaling and role of intermittency," Astrophys. J. **702**, 537 (2009).
[15]J. Podesta, D. Roberts, and M. Goldstein, "Spectral exponents of kinetic and magnetic energy spectra in solar wind turbulence," Astrophys. J. **664**, 543 (2007).
[16]J. Podesta, B. D. Chandran, A. Bhattacharjee, D. Roberts, and M. Goldstein, "Scale-dependent angle of alignment between velocity and magnetic field fluctuations in solar wind turbulence," J. Geophys. Res.: Space Phys. **114**, A01107, https://doi.org/10.1029/2008JA013504 (2009).
[17]J. M. Weygand, W. Matthaeus, S. Dasso, M. Kivelson, and R. Walker, "Taylor scale and effective magnetic Reynolds number determination from plasma sheet and solar wind magnetic field fluctuations," J. Geophys. Res.: Space Phys. **112**, A10201, https://doi.org/10.1029/2007JA012486 (2007).
[18]A. Pouquet, D. Rosenberg, and J. E. Stawarz, "Interplay between turbulence and waves: Large-scale helical transfer, and small-scale dissipation and mixing in fluid and Hall–MHD turbulence," Rend. Lincei, Sci. Fis. Nat. **31**, 949 (2020).
[19]A. Pouquet, J. E. Stawarz, and D. Rosenberg, "Coupling large eddies and waves in turbulence: Case study of magnetic helicity at the ion inertial scale," Atmosphere **11**, 203 (2020).
[20]D. Falceta-Gonçalves, G. Kowal, E. Falgarone, and A.-L. Chian, "Turbulence in the interstellar medium," Nonlinear Processes Geophys. **21**, 587 (2014).
[21]M. J. Lighthill, "Studies on magneto-hydrodynamic waves and other anisotropic wave motions," Philos. Trans. R. Soc. London, Ser. A **252**, 397 (1960).
[22]D. O. Gómez, P. D. Mininni, and P. Dmitruk, "Hall-magnetohydrodynamic small-scale dynamos," Phys. Rev. E **82**, 036406 (2010).
[23]B. Hnat, S. C. Chapman, and G. Rowlands, "Compressibility in solar wind plasma turbulence," Phys. Rev. Lett. **94**, 204502 (2005).
[24]T. S. Horbury, M. Forman, and S. Oughton, "Anisotropic scaling of magnetohydrodynamic turbulence," Phys. Rev. Lett. **101**, 175005 (2008).
[25]L. N. Martin, P. Dmitruk, and D. O. Gomez, "Energy spectrum, dissipation, and spatial structures in reduced Hall magnetohydrodynamic," Phys. Plasmas **19**, 052305 (2012).
[26]P. D. Mininni, D. O. Gómez, and S. M. Mahajan, "Dynamo action in Hall magnetohydrodynamics," Astrophys. J. Lett. **567**, L81 (2002).
[27]P. D. Mininni, D. O. Gómez, and S. M. Mahajan, "Dynamo action in magnetohydrodynamics and Hall-magnetohydrodynamics," Astrophys. J. **587**, 472 (2003).
[28]P. D. Mininni, D. O. Gómez, and S. M. Mahajan, "Direct simulations of helical Hall–MHD turbulence and dynamo action," Astrophys. J. **619**, 1019 (2005).
[29]P. D. Mininni, A. Alexakis, and A. Pouquet, "Energy transfer in Hall–MHD turbulence: Cascades, backscatter, and dynamo action," J. Plasma Phys. **73**, 377 (2007).
[30]G. Boffetta, A. Celani, A. Crisanti, and R. Prandi, "Intermittency of two-dimensional decaying electron magnetohydrodynamic turbulence," Phys. Rev. E **59**, 3724 (1999).
[31]S. Chapman, B. Hnat, and K. Kiyani, "Solar cycle dependence of scaling in solar wind fluctuations," Nonlinear Processes Geophys. **15**, 445 (2008).
[32]D. Shaikh and P. Shukla, "3D simulations of fluctuation spectra in the Hall-MHD plasma," Phys. Rev. Lett. **102**, 045004 (2009).
[33]D. Hori and H. Miura, "Spectrum properties of Hall MHD turbulence," Plasma Fusion Res. **3**, S1053 (2008).
[34]H. Miura and K. Araki, "Structure transitions induced by the Hall term in homogeneous and isotropic magnetohydrodynamic turbulence," Phys. Plasmas **21**, 072313 (2014).
[35]H. Miura, K. Araki, and F. Hamba, "Hall effects and sub-grid-scale modeling in magnetohydrodynamic turbulence simulations," J. Comput. Phys. **316**, 385 (2016).
[36]H. Miura and K. Araki, "Coarse-graining study of homogeneous and isotropic Hall magnetohydrodynamics turbulence," Plasma Phys. Controlled Fusion **55**, 014012 (2013).
[37]H. Miura, J. Yang, and T. Gotoh, "Hall magnetohydrodynamic turbulence with a magnetic Prandtl number larger than unity," Phys. Rev. E **100**, 063207 (2019).
[38]D. Banerjee, S. S. Ray, G. Sahoo, and R. Pandit, "Multiscaling in Hall-magnetohydrodynamic turbulence: Insights from a shell model," Phys. Rev. Lett. **111**, 174501 (2013).
[39]S. Galtier and E. Buchlin, "Multiscale Hall-magnetohydrodynamic turbulence in the solar wind," Astrophys. J. **656**, 560 (2007).
[40]S. Galtier, "von Kármán–Howarth equations for Hall magnetohydrodynamic flows," Phys. Rev. E **77**, 015302 (2008).
[41]R. Meyrand and S. Galtier, "Spontaneous chiral symmetry breaking of Hall magnetohydrodynamic turbulence," Phys. Rev. Lett. **109**, 194501 (2012).
[42]R. Meyrand, K. H. Kiyani, Ö. D. Gürcan, and S. Galtier, "Coexistence of weak and strong wave turbulence in incompressible Hall magnetohydrodynamics," Phys. Rev. X **8**, 031066 (2018).
[43]V. Krishan and S. Mahajan, "Magnetic fluctuations and Hall magnetohydrodynamic turbulence in the solar wind," J. Geophys. Res.: Space Phys. **109**, A11105, https://doi.org/10.1029/2004JA010496 (2004).
[44]D. O. Gómez, P. D. Mininni, and P. Dmitruk, "MHD simulations and astrophysical applications," Adv. Space Res. **35**, 899 (2005).
[45]W. H. Matthaeus and P. Dmitruk, "Impact of Hall effect on energy decay in magnetohydrodynamic turbulence," Geophys. Res. Lett. **30**, 2104, https://doi.org/10.1029/2003GL017949 (2003).
[46]D. Smith, S. Ghosh, P. Dmitruk, and W. H. Mathaeus, "Hall and turbulence effects on magnetic reconnection," Geophys. Res. Lett. **31**, L02805, https://doi.org/10.1029/2003GL018689 (2004).
[47]D. Hori, M. Furukawa, S. Ohsaki, and Z. Yoshida, "A shell model for the Hall MHD system," J. Plasma Fusion Res. **81**, 141 (2005).

[48]D. Chae, P. Degond, and J.-G. Liu, "Well-posedness for Hall-magneto-hydrodynamics," Ann. IHP Anal. Non Linéaire **31**, 555–565 (2014).
[49]A. Alghamdi, S. Gala, and M. Ragusa, "A regularity criterion of smooth solution for the 3D viscous Hall-MHD equations," AIMS Math. **3**, 565 (2018).
[50]M. L. Goldstein, D. Roberts, and W. Matthaeus, "Magnetohydrodynamic turbulence in the solar wind," Annu. Rev. Astron. Astrophys. **33**, 283 (1995).
[51]M. K. Verma, "Nonclassical viscosity and resistivity of the solar wind plasma," J. Geophys. Res.: Space Phys. **101**, 27543, https://doi.org/10.1029/96JA02324 (1996).
[52]R. Bruno and V. Carbone, "The solar wind as a turbulence laboratory," Living Rev. Sol. Phys. **10**, 2 (2013).
[53]R. Bruno and V. Carbone, *Turbulence in the Solar Wind* (Springer, 2016), Vol. 928.
[54]K. Kiyani, S. Chapman, Y. V. Khotyaintsev, M. Dunlop, and F. Sahraoui, "Global scale-invariant dissipation in collisionless plasma turbulence," Phys. Rev. Lett. **103**, 075006 (2009).
[55]W. H. Matthaeus and M. L. Goldstein, "Measurement of the rugged invariants of magnetohydrodynamic turbulence in the solar wind," J. Geophys. Res.: Space Phys. **87**, 6011, https://doi.org/10.1029/JA087iA08p06011 (1982).
[56]W. H. Matthaeus, M. Wan, S. Servidio, A. Greco, K. T. Osman, S. Oughton, and P. Dmitruk, "Intermittency, nonlinear dynamics and dissipation in the solar wind and astrophysical plasmas," Philos. Trans. R. Soc. A: Math., Phys. Eng. Sci. **373**, 20140154 (2015).
[57]O. Alexandrova, C. H. K. Chen, L. Sorriso-Valvo, T. S. Horbury, and S. D. Bale, "Solar wind turbulence and the role of ion instabilities," Space Sci. Rev. **178**, 101 (2013).
[58]F. Sahraoui, L. Hadid, and S. Huang, "Magnetohydrodynamic and kinetic scale turbulence in the near-earth space plasmas: A (short) biased review," Rev. Mod. Plasma Phys. **4**, 4 (2020).
[59]O. Alexandrova, V. Carbone, P. Veltri, and L. Sorriso-Valvo, "Small-scale energy cascade of the solar wind turbulence," Astrophys. J. **674**, 1153 (2008).
[60]O. Alexandrova, V. Carbone, P. Veltri, and L. Sorriso-Valvo, "Solar wind cluster observations: Turbulent spectrum and role of Hall effect," Planet. Space Sci. **55**, 2224 (2007).
[61]G. Zimbardo, A. Greco, L. Sorriso-Valvo, S. Perri, Z. Vörös, G. Aburjania, K. Chargazia, and O. Alexandrova, "Magnetic turbulence in the geospace environment," Space Sci. Rev. **156**, 89 (2010).
[62]U. Frish, *Turbulence: The Legacy of A. N. Kologorov* (Cambridge University Press, Cambridge, England, 1995).
[63]B. J. Vasquez, V. I. Abramenko, D. K. Haggerty, and C. W. Smith, "Numerous small magnetic field discontinuities of Bartels rotation 2286 and the potential role of Alfvénic turbulence," J. Geophys. Res.: Space Phys. **112**, A11102, https://doi.org/10.1029/2007JA012504 (2007).
[64]W. H. Matthaeus, D. C. Montgomery, M. Wan, and S. Servidio, "A review of relaxation and structure in some turbulent plasmas: Magnetohydrodynamics and related models," J. Turbul. **13**, N37 (2012).
[65]P. D. Mininni, A. G. Pouquet, and D. C. Montgomery, "Small-scale structures in three-dimensional magnetohydrodynamic turbulence," Phys. Rev. Lett. **97**, 244503 (2006).
[66]S. A. Orszag and C.-M. Tang, "Small-scale structures of two-dimensional magnetohydrodynamic turbulence," J. Fluid Mech. **90**, 129 (1979).
[67]M. Wan, K. T. Osman, W. H. Matthaeus, and S. Oughton, "Investigation of intermittency in magnetohydrodynamics and solar wind turbulence: Scale-dependent kurtosis," Astrophys. J. **744**, 171 (2012).
[68]E. Papini, L. Franci, S. Landi, A. Verdini, L. Matteini, and P. Hellinger, "Can Hall magnetohydrodynamics explain plasma turbulence at sub-ion scales," Astrophys. J. **870**, 52 (2019).
[69]P. Rodriguez Imazio, L. N. Martin, P. Dmitruk, and P. D. Mininni, "Intermittency in Hall-magnetohydrodynamics with a strong guide field," Phys. Plasmas **20**, 052506 (2013).
[70]V. Dallas and A. Alexakis, "Structures and dynamics of small scales in decaying magnetohydrodynamic turbulence," Phys. Fluids **25**, 105106 (2013).
[71]L. Turner, "Hall effects on magnetic relaxation," IEEE Trans. Plasma Sci. **14**, 849 (1986).
[72]R. Bandyopadhyay, W. H. Matthaeus, T. N. Parashar, Y. Yang, B. L. Giles, D. J. Gershman, C. J. Pollock, C. T. Russell, R. J. Strangeway, R. B. Torbert, T. E. Moore, and J. L. Burch, "Statistics of kinetic dissipation in the earth's magneto-sheath: MMS observations," Phys. Rev. Lett. **124**, 255101 (2020).
[73]R. Pandit, P. Perlekar, and S. S. Ray, "Statistical properties of turbulence: An overview," Pramana **73**, 157 (2009).
[74]R. Benzi, S. Ciliberto, R. Tripiccione, C. Baudet, F. Massaioli, and S. Succi, "Extended self-similarity in turbulent flows," Phys. Rev. E **48**, R29 (1993).
[75]S. Chakraborty, U. Frisch, and S. S. Ray, "Extended self-similarity works for the burgers equation and why," J. Fluid Mech. **649**, 275 (2010).
[76]A. D. Rosis, R. Liu, and A. Revell, "One-stage simplified lattice Boltzmann method for two- and three-dimensional magnetohydrodynamics flows," Phys. Fluids **33**, 085114 (2021).
[77]A. D. Rosis, J. Al-Adham, H. Al-Ali, and R. Meng, "Double-D2Q9 lattice Boltzmann models with extended equilibrium for two-dimensional magneto-hydrodynamic flows," Phys. Fluids **33**, 035143 (2021).